

Lappeenranta–Lahti University of Technology LUT
School of Energy Systems
Degree Programme in Electrical Engineering

Matti Salervo

**INSTRUMENTATION ELECTRONICS
FOR A NOVEL OPTICAL GAS SENSOR**

Master's Thesis

Examiners: Prof. Pertti Silventoinen
M.Sc. (Tech.) Markus Huuhtanen

ABSTRACT

Lappeenranta–Lahti University of Technology LUT
School of Energy Systems
Degree Programme in Electrical Engineering

Matti Salervo

INSTRUMENTATION ELECTRONICS FOR A NOVEL OPTICAL GAS SENSOR

Master's Thesis

2020

88 pages, 40 figures, 5 tables, 1 appendix.

Examiners: Prof. Pertti Silventoinen
M.Sc. (Tech.) Markus Huuhtanen

Keywords: analog electronics, analog signal processing, electronics design, infrared spectroscopy, optical gas sensing, photodetector, printed circuit board design

Optical gas sensors are measuring instruments that can be used to determine the concentration of various gases, such as carbon dioxide. They are widely utilized in many areas of industry. In this master's thesis commissioned by Vaisala Oyj, instrumentation electronics and a printed circuit board were designed for a novel optical nondispersive infrared gas sensor prototype. Previously designed separate test circuits were used as a basis for the design work done. The research objective of the thesis was approached by utilizing the applicable parts of the design science research method. A functioning single-circuit-board prototype device was achieved as the main result of the work done. The main features of the prototype were experimentally tested. In the end, after small modifications made, the prototype's subassemblies operated as planned. Further research is needed especially to optimize the electronics and the printed circuit board design, as well as to define the actual performance of the prototype by using it to measure known target gas concentrations.

TIIVISTELMÄ

Lappeenrannan–Lahden teknillinen yliopisto LUT
School of Energy Systems
Sähkötekniikan koulutusohjelma

Matti Salervo

INSTRUMENTOINTIELEKTRONIIKAN TOTEUTUS UUDENLAISTA OPTISTA KAASUANTURIA VARTEN

Diplomityö

2020

88 sivua, 40 kuvaa, 5 taulukkoa, 1 liite.

Työn tarkastajat: Prof. Pertti Silventoinen
DI Markus Huuhtanen

Hakusanat: analogiaelektroniikka, analogiasignaalin käsittely, elektroniikkasuunnittelu, fotodetektorit, infrapunaspektroskopia, optiset kaasumittaukset, piirilevysuunnittelu

Optiset kaasuanturit ovat mittausrakenteita, joita voidaan käyttää monien eri kaasujen, kuten hiilidioksidin, konsentraation määrittämiseen. Niitä hyödynnetään laajamittaisesti useilla teollisuuden aloilla. Tässä Vaisala Oyj:n toimeksiannosta tehdyssä diplomityössä suunniteltiin instrumentointielektroniikka sekä piirilevy uudenlaisen optisen ei-dispersiivisen infrapunakaasuanturin prototyyppiä varten. Tehdyn suunnittelutyön pohjana käytettiin aikaisemmin suunniteltuja toisistaan erillisiä testipiirejä. Tutkimuksen tavoitetta lähestyttiin hyödyntämällä suunnittelutieteellistä tutkimusmenetelmää sen soveltuvilta osin. Työn tärkein tulos on osana sitä toteutettu toiminnallinen yhden piirilevyn prototyyppilaitte. Prototyypin pääominaisuuksia testattiin kokeellisesti. Pienten muutosten jälkeen prototyypin osakokonaisuuksien todettiin toimivan suunnitellusti. Jatkotutkimusta tarvitaan erityisesti suunnitellun elektroniikan ja piirilevyn optimoimiseksi, sekä prototyypin suorituskyvyn määrittämiseksi tunnettuja kohdekaasun pitoisuuksia mittaamalla.

PREFACE

I would first like to thank the examiners of this thesis, as well as all of my colleagues, for their invaluable contribution to this work. Thank you professor Silventoinen for all the tips and feedback regarding general arrangements and academic writing. Thank you Markus H. and Asko N. for assisting me with the electronics design, Marko H. for the embedded software and Esa K. for the mechanics. I would also like to collectively thank my superiors and the whole of Vaisala Oyj for providing me this wonderful opportunity. This company is filled with truly amazing people; kind souls that are absolute top talents of their versatile areas of expertise. It has been a genuine pleasure to begin my career by being a part of this laid-back yet highly professional community.

To my family; thank you for unconditionally supporting me throughout all these years, even during the most difficult and uncertain times. The encouragement I have received from you means the world to me. To Sakari, Krister, Ossi, J-P and all of my other dear friends & fellow students from the LUT department of Electrical Engineering; I would never have made it academically this far without you – thank you for *everything*.

I would like to dedicate this work to my fiancée Karoliina and my son Väinö – there are no words to express my gratitude for all the understanding, support, love and joy that both of you have given to me throughout the process of writing this thesis and all the years I have been blessed to spend with you.

Vantaanlaakso, July 18, 2020



Matti Salervo

CONTENTS

1	INTRODUCTION	8
1.1	Background & motivation	9
1.2	Objectives & delimitations	10
1.3	Research methods & materials	11
1.4	Structure of the thesis	11
2	ABSORPTION SPECTROSCOPY	12
2.1	Electromagnetic spectrum & absorption of radiation	12
2.2	Infrared absorption spectroscopy	15
2.3	Infrared radiation emitters	17
2.3.1	Electroluminescent sources	18
2.3.2	Incandescent sources	19
2.4	Optical filters	21
2.5	Infrared detectors	23
2.5.1	Thermal detectors	23
2.5.2	Photonic detectors	25
3	ELECTRONICS THEORY	28
3.1	Operational amplifiers	28
3.2	Analog-to-digital converters	31
3.3	DC voltage regulators	32
3.4	Infrared signal modulation	33
3.5	Thermoelectric cooling	34
3.6	Digital control	36
4	ELECTRONICS DESIGN	38
4.1	Passive components	40
4.2	Control of infrared source & tunable optical filter	40
4.3	Infrared photodetectors	41
4.3.1	Detector type 1: VIGO System PVIA-2TE- λ_{opt}	42
4.3.2	Detector type 2: Hamamatsu Photonics P13243	43
4.4	Photodetector signal amplification	45
4.4.1	Stage 1: transimpedance amplifier	45
4.4.2	Stage 2: inverting amplifier	47
4.4.3	Design verification by simulation	48
4.5	Detector temperature control	49
4.5.1	General setup	50

	6
4.5.2	Thermistor linearization 52
4.5.3	Control signal filter 55
4.5.4	Heat dissipation 56
4.6	Microcontroller unit 58
4.7	Supply & operating voltages 59
5	PRINTED CIRCUIT BOARD DESIGN 62
5.1	General requirements & design rules 62
5.2	Layer setup & interconnections 63
5.3	Component layout & routing 64
5.4	Automated error checking 66
6	EVALUATING OPERATION OF THE PROTOTYPE 67
6.1	Description of experiments 67
6.2	Measurement setups 68
6.3	Results & discussion 69
6.4	Future work 76
7	CONCLUSION 78
	REFERENCES 79
	APPENDICES
	Appendix 1: MCU Pin Configuration

LIST OF SYMBOLS & ABBREVIATIONS

A	Absorbance, Amplification, Area
C	Concentration [M]
D*	Specific Detectivity [$\text{cmHz}^{1/2}\text{W}^{-1}$, Jones]
I	Radiation Intensity [$\frac{\text{W}}{\text{cm}^2}$]
k	Absorption Coefficient [$\text{M} \cdot \text{cm}^{-1}$]
L	Optical Path Length [cm]
NEP	Noise Equivalent Power [$\text{W}/\sqrt{\text{Hz}}$]
S	Photosensitivity [A/W, V/W]
λ, λ_p	Wavelength, Peak Sensitivity Wavelength [μm]
μG	Microglow; a Vaisala-Patented Silicon MEMS Emitter Infrared Source
$\Sigma\Delta$	Sigma-Delta, a Subcategory of Analog-to-Digital Converters
τ	Response Time, Time Constant [ms, ns]
A/D	Analog-to-Digital
ADC	Analog-to-Digital Converter
ASIC	Application-Specific Integrated Circuit
EM	Electromagnetic
FIR	Far Infrared (15-1000 μm)
FPI	Fabry-Pérot Interferometer
IR	Infrared
LED	Light-emitting Diode
LWIR	Long-Wavelength Infrared (8-15 μm)
MCU	Microcontroller Unit
MEMS	Microelectromechanical System
MWIR	Mid-Wavelength Infrared (3-8 μm)
NDIR	Nondispersive Infrared
NIR	Near Infrared (0.75-1.40 μm)
NTC	Negative Temperature Coefficient
OP-AMP	Operational Amplifier
PCB	Printed Circuit Board
PID	Proportional—Integral—Derivative
PWM	Pulse-Width Modulation
SNR	Signal-to-Noise Ratio
SWIR	Short-Wavelength Infrared (1.40-3.00 μm)
TEC	Thermoelectric Cooler
TIA	Transimpedance Amplifier
TO	Transistor Outline; a Component Package Type

1 INTRODUCTION

Interestingly, the practice of using canary birds for detecting hazardous gases inside coal mines had not been completely stopped in the United Kingdom until as recently as just a few decades ago [1]. As seen in figure 1 [2], not only birds but also other small animals like rabbits have been historically used for similar kinds of purposes. This is because smaller animals typically react to considerably lower concentrations of many lethal gases than humans do [3], thus offering their possessor an opportunity to escape from the danger zone or take other measures required to normalize the situation.

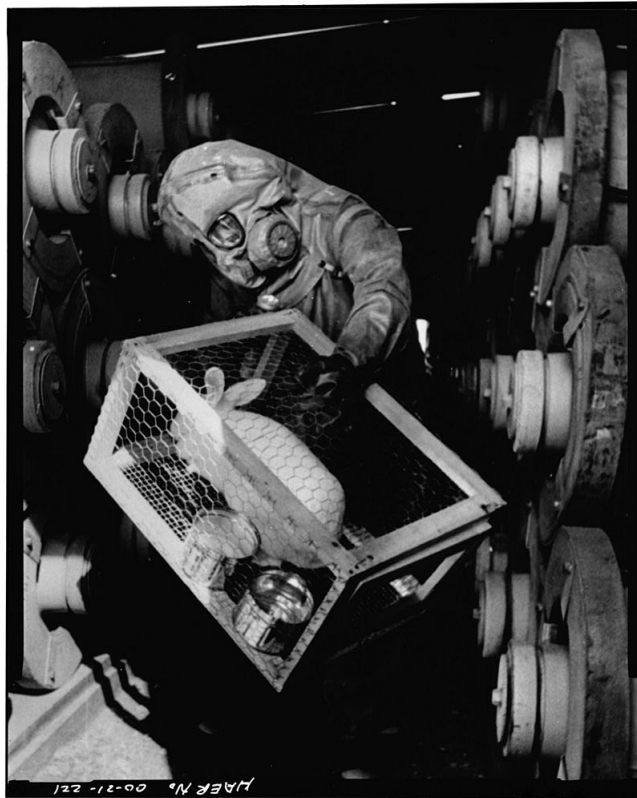


Figure 1. A 1970's public domain photograph by a Denver Post photographer, showing a caged rabbit being used to monitor for potential sarin gas leaks at a chemical plant manufacturing the notorious nerve agent. The figure is retrieved from [2].

Fortunately for the canaries and other sentinel species alike, scientists and engineers have invented more accurate and reliable methods for detecting and monitoring the concentration of many types of gases [4]. One of these modern methods, or branches of technology, is optical gas sensing. It should be noted that the aforementioned mining industry certainly is not the only utilizer of this technology. Instead, many kinds of optical gas

sensors are used for a wide variety of applications in different fields of industry, such as building automation, life sciences, process safety and food industry. Optical gas sensors can be sorted into subcategories based on their operating principle. This thesis focuses on nondispersive infrared sensing, which is an absorption-based optical gas sensing technology - however, it is notable that also non-absorption-based gas sensing technologies exist and are well suited for some applications, like low-concentration ambient air quality measurements [5].

Due to their highly application-specific nature, it would be difficult to make substantiated claims that there would be distinguishable technology-wide historical turning points in the development of optical gas sensors. Not any single method has been able to stand out and gain a significant market share in the industry [6], instead the perception created by the different commercial actors in the field - as well as actual customer need for certain features - has dominantly guided the development work towards multiple directions that have changed over time due to changes in the industry. In practice this could mean, for example, pursuing for miniaturization of a device or the objective of trying to achieve a higher accuracy or a wider measuring range [6]. Pursuit of improved performance of an existing technology is essentially the goal of this thesis too, as described later in this chapter.

1.1 Background & motivation

At Vaisala Oyj (hereinafter referred to as Vaisala) both new applications for existing measurement technologies and new measurement technologies for existing and potentially profitable applications are constantly being studied and developed. The company invests significantly in research and development; at the time of writing up to 13% of the company's net sales is invested in R&D and about 22% of the ca. 1,800 Vaisala employees worldwide work within R&D activities [7,8]. At the Vaisala Industrial Measurements department, versatile development work related to the CARBOCAP[®] optical nondispersive infrared gas sensing technology has been done over the years. One of the many aspects of the development work is to shorten the response time as well as to further improve measurement sensitivity. This type of rapid yet highly responsive optical gas measurement technology has several interesting potential applications related to both industrial and environmental measurements, including but not limited to the uninterruptedly moving production lines of food and beverage industries, and monitoring fluxes of certain gases related to background air quality and agriculture [5,9]. This thesis acts as a step towards the commercialization of the rapid CARBOCAP[®] technology.

1.2 Objectives & delimitations

The research objective of this master's thesis is to design and implement electronics for a prototype measuring instrument used for optical gas measurements. Most subsystems of the concept have been proven to work but tests with known gas concentrations have not been done yet. Thus, the previously created separate prototypes of the different subsystems will be combined to form a stand-alone single-circuit-board solution. This allows performance evaluation of the concept through measurements of known target gas concentrations. As a new feature, control electronics required for the temperature control of the detectors used will be added onboard to complement the trial designs implemented so far - in the past, a separate bench top device (Thorlabs TED200C) has been used for this purpose. The prototype consists of a custom-made optical cuvette, and a printed circuit board (PCB) containing the following electrical subsystems:

- A Vaisala Microglow (μG) IR source & a voltage-tunable optical Fabry–Pérot interferometer (FPI) filter and the control electronics required to operate them.
- A photodiode-based infrared (IR) detector - two alternatives are tested.
- Amplification of the measurement signal produced by the detector.
- Control & driver electronics for thermoelectric cooler (TEC) modules integrated inside both of the detectors used.
- A multi-purpose microcontroller unit (MCU) for the analog-to-digital (A/D) conversion & conditioning of the measurement signal and for controlling the prototype.
- RS-232 serial bus that enables flashing & commanding the MCU, as well as logging measurement data using a command-line interface on a personal computer.
- Power management, including the main supply voltage inputs and regulating the initial input voltage to the smaller voltage levels, as well as boosting the initial input voltage to the higher voltage levels required.
- Passive electromagnetic interference protection & filtering.

This thesis does not consider the optomechanical design (including the mechanical design of the optical cuvette, type[s] of the mirror[s] used, component alignment, focusing, et cetera) of the prototype. In addition, embedded software development necessary for operating the prototype will be fully excluded from the scope of this work due to the limited schedule. Any work related to these topics is to be completely taken care of by other engineers of the Vaisala Industrial Measurements unit.

1.3 Research methods & materials

The research objective is approached by making use of the seven guidelines of the design science research method, proposed by Havner et al. in [10], to the extent applicable. This outcome-based research method should be well-suited for the purpose of this thesis considering that the objective of the thesis is to produce a novel artifact (a prototype device) that is designed to improve the performance of existing technology, in the same manner as Havner et al. describe the method [10].

Literary information related to the basic theory background of the field of research of this thesis is acquired from various fundamental literary works, such as books released by academic publishers, scientific journal articles, conference proceedings as well as thesis publications. Reference is also made to various articles and other material that is available online. In addition to the academic publications and online materials, application notes released by electronics manufacturers and datasheets of the electronic components chosen are used as a reference for the design work done. The design work is partly based on proprietary Vaisala prototype designs and experiential knowledge of the company's electronics engineers. At the request of the company, efforts were made to use previously utilized components as well as suppliers to the extent possible.

1.4 Structure of the thesis

This thesis is divided into seven main chapters. First, in Chapter 1, the topic of the work is described at a general level and the background, objectives and delimitation of the thesis are introduced. Then, in Chapter 2, the fundamental theory of absorption spectroscopy is explained and some components typically used and their operating principles are presented. The 3rd Chapter examines the theory of electronics relevant to the design work done, as well as the electrical properties related to the essential components used. After that, Chapters 4 and 5 describe the prototype instrumentation electronics and the PCB designed, respectively. In Chapter 6, the measurements performed using the prototype and the results obtained are described and discussed. Furthermore, the results are evaluated and proposals for future work are revealed. Finally, Chapter 7 concludes the work.

2 ABSORPTION SPECTROSCOPY

This chapter introduces the theory background related to absorption spectroscopy, beginning from describing the essential concepts and ending to an introduction and comparison of selected electronic and optical components suitable to be used in optical gas measurements. It should first be noted that there are many other gas sensing technologies in addition to optical gas sensing. These include various methods based on observing changes in the electrical properties of the material used for detection, like the electrochemical cells, and many other less common methods, like calorimetric and acoustic gas detectors [11]. This thesis focuses on spectroscopy, which is a field of research and technology that utilizes the study of how electromagnetic (EM) radiation interacts with matter [12]. More specifically, as described by Kumar [13], absorption spectroscopy is one of the three main branches of spectroscopy and deals with how electromagnetic radiation is absorbed at different wavelengths - the remaining two branches, scattering spectroscopy and emission spectroscopy, are not relevant to this thesis and are thus ignored. The concept of absorption spectroscopy also includes the versatile variety of methods used to perform absorption-spectrometric measurements.

2.1 Electromagnetic spectrum & absorption of radiation

EM radiation is a form of energy that behaves both like particles and waves do [14]. EM radiation is divided into different regions, called bands, that correspond to all the different wavelengths and frequencies of it. These bands together form the spectrum of electromagnetic radiation, seen in figure 2 [15]. The bands of EM spectrum include gamma radiation (γ -rays), X-radiation (X-rays), ultraviolet (UV), the visible spectrum, infrared (IR), microwaves and radio waves. As the Planck–Einstein relation suggests, the shorter the wavelength of EM radiation, the higher its frequency and energy [16]. Partly because of this relation, very low or very high energy EM radiation cannot be widely utilized in absorption spectroscopy; low-energy radiation may not be sufficient to change the energy state of the observed substance, and too high an energy could lead to ionization of the substance.

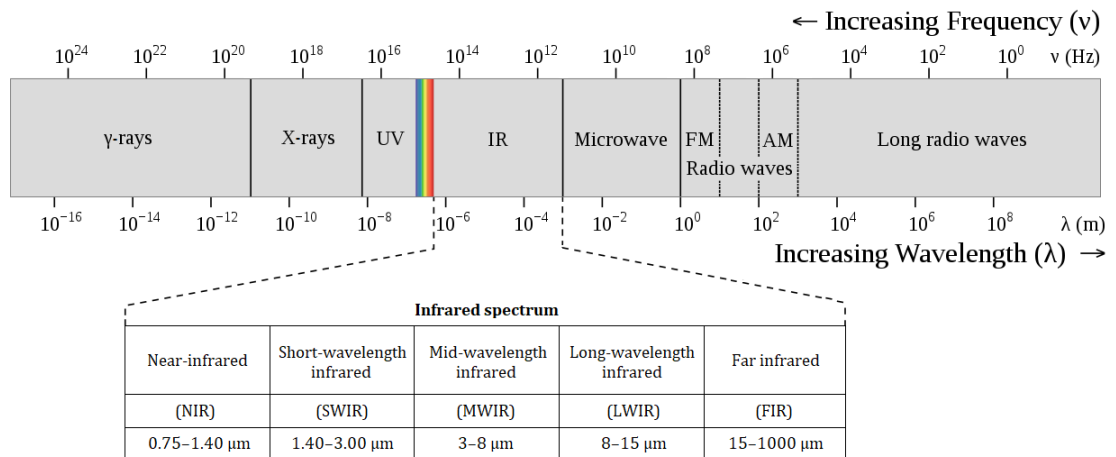


Figure 2. The electromagnetic spectrum and its different bands, with the IR band highlighted. The IR region is unraveled and defined in more detail as described in [17]. The figure is an adaptation of [15], retrieved and modified under the CC BY-SA 3.0 license.

Nevertheless, most of the bands of EM radiation can be used for absorption spectroscopy, though some of the bands are only suitable for highly specialized applications and are used solely for the purpose of scientific research. Table 1 [13] lists the most common types of absorption spectroscopy and their respective bands of EM radiation.

Table 1. Main types of absorption spectroscopy. [13]

Band of EM Radiation	Spectroscopic Type
X-ray	X-ray Absorption Spectroscopy
UV–Vis	Ultraviolet–Visible Absorption Spectroscopy
IR	Infrared Absorption Spectroscopy
Microwave	Microwave Absorption Spectroscopy
Radio wave	Electron Spin Resonance Spectroscopy, Nuclear Magnetic Resonance Spectroscopy

X-ray & microwave absorption spectroscopy have a limited number of industrial applications (for example, some related to microelectronics processing technology, healthcare technology and analytical chemistry [18–20]), whereas applications of radio wave absorption spectroscopy are almost exclusively related to scientific research, such as astronomy [21]. In turn, the most significant commercially exploited bands of EM radiation are

UV/Visible and IR. Some examples of the users/uses of UV–Vis absorption spectroscopy would be the cosmetic industry, food & agriculture industry, and qualitative & quantitative analysis performed in the pharmaceutical industry. It should be noted that not as many gases absorb energy on the UV–Vis band as on the IR band. A few examples of IR absorption spectroscopy would be a variety of measurements performed for dynamic quantities, long-term monitoring of gaseous substances, as well as industrial automation & process control. Some commonly measured gases absorbing at the IR band include carbon monoxide (CO), carbon dioxide (CO₂), sulfur dioxide (SO₂), nitrogen oxides (NO_x), nitrous oxide (N₂O), ammonia (NH₃), hydrogen chloride (HCl), hydrogen fluoride (HF), methane (CH₄), et cetera [22].

When EM radiation passes through a gaseous medium, may it consist of either atoms or molecules, most of the radiation passes through losslessly. Nonetheless, at some substance-specific wavelengths, the intensity of the incident radiation decreases, as energy is absorbed into the chemical substance the medium consists of. When energy is absorbed, the atoms or molecules contained in the medium move from their baseline energy state to a more energetic, excited state. The type of transition of the energy state (e.g. electronic transition or molecular vibration/rotation) depends on the energy of the photons in the EM radiation, which in turn is related to the wavelength of the radiation. Figure 3 [23] shows the IR absorption bands of a few gases. Worth noting is that some substances absorb at overlapping wavelengths, which can cause measurement interference. [13]

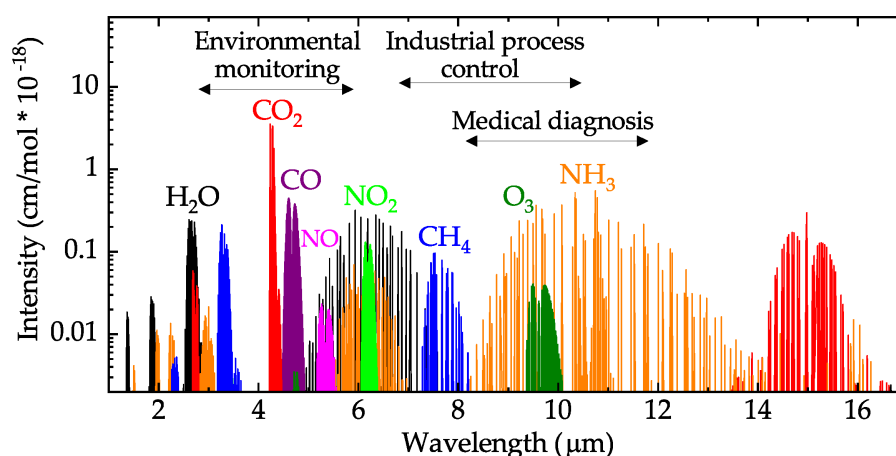


Figure 3. IR absorption spectra of certain gases used in industrial applications. Some typical applications are named and their respective wavelength ranges highlighted using double-headed arrows. The figure is retrieved from [23] under the CC BY 4.0 license.

Especially water (H₂O) absorbs IR radiation over a very wide wavelength range and overlaps with the absorption bands of many other substances. Whenever overlapping absorption wavelengths are used for measuring, the need for compensation is created [22]. Compensation can be carried out for example by introducing a reference measurement to the system. Unfortunately, this would make the system more complex and increase the sources of measurement uncertainty, so whenever possible, a non-overlapping wavelength should be chosen to reduce the risk of cross-sensitivity.

As highlighted throughout this section, many chemical substances having some use in industrial applications absorb on the IR band. This makes IR absorption spectroscopy an attractive subject for commercial research and development.

2.2 Infrared absorption spectroscopy

IR absorption spectroscopy can roughly cover the portion of the EM spectrum that sets in between the near-infrared (NIR) and the long-wavelength infrared (LWIR) regions. The corresponding endpoint wavelengths for these two IR bands are approximately 0.75 μm and 15.0 μm [17], depending on the definition. Some of the IR bands are naturally useful for a larger number of applications than others, as the absorption bands of the different target materials, substances and compounds are not evenly distributed along the IR spectrum [24]. Many gases strongly absorb at the mid-wavelength infrared (MWIR) band [25]. IR absorption spectroscopy is suitable for many kinds of scientific and industrial applications of both qualitative and quantitative type, such as compound characterization and optical gas measurements. The latter of these two applications has produced a broad family of measurement devices designed to detect a certain gas and measure the concentration of it. Some of the state-of-the-art devices are capable of accurately measuring multiple different gases [26].

Nondispersive infrared (NDIR) sensors are among the most widely used types of optical gas measurement sensors. In practice, NDIR means that the IR radiation used to perform the measurement does not disperse while traveling through the sensor and the gaseous medium, meaning that no prism-like scatter-causing optics are used. Compared to the dispersive IR sensors commonly used in analytical chemistry, NDIR sensors are used for a different purpose and are simpler in structure [27]. Figure 4 [28] shows the key components of a typical NDIR sensor used for optical gas measurements.

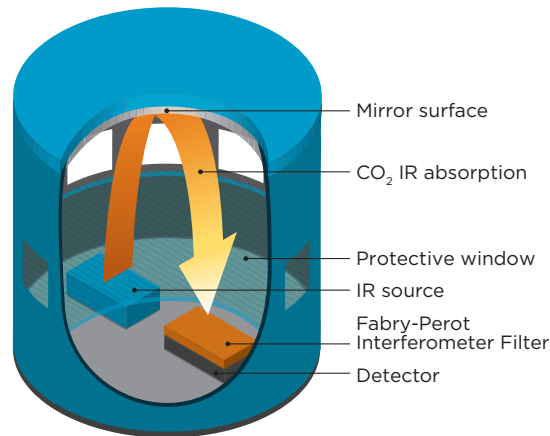


Figure 4. An illustration of the structure of Vaisala CARBOCAP[®] sensor and the key components of it. The structure seen is, for the most part, quite typical for NDIR sensors. [28]

These devices typically include: 1. an IR source, 2. an IR detector, and 3. some optical filtering and other optics, such as mirror[s]. Lastly, some form of an optical cuvette is often used as the waveguide and a mounting base for the electronics and the introduced components 1.-3. Now let us break down and refine each of these typically used components and their purpose. First, in order to accomplish the desired excitation of the gaseous molecules of interest, as introduced in section (2.1), an IR source (also called an IR *emitter*) has to be utilized. Then, at least one optical filter, be it of fixed-bandpass or tunable type, is usually placed somewhere within the optical path between the emitter and detector components to make it possible to distinguish the absorption caused by the target gas from that of other gases that could otherwise interfere with the measurement. It is quite common to use several filters to separate the reference and absorption bands. Mirrors or other optics can be used to compactly increase the length of the optical path between the emitter and detector components, allowing for lower concentrations of target gases to be detected. Finally, a detector is required to observe the signal initially transmitted by the emitter, and to detect the decrease in radiation intensity caused by the absorption of energy. Modern NDIR sensors virtually always include some computing power too, as a wide variety of small-sized embedded microprocessors are nowadays available at several different price categories. Some of the microprocessors available are specifically designed for measurement applications.

NDIR spectroscopy is based on the Beer–Lambert–Bouguer law, which combines the decrease in radiation intensity (caused by absorption of radiant energy) with the material properties of a substance. This makes it possible to calculate the concentration of a target gas within a constant optical distance. The equation can be represented in the following form:

$$\begin{cases} \frac{I}{I_0} = e^{-k \cdot C \cdot L} \\ A = \ln \left(\frac{I_0}{I} \right) \end{cases} \quad (1)$$

where I [$\frac{\text{W}}{\text{cm}^2}$] is the radiation intensity after passing through the sample gas, I_0 [$\frac{\text{W}}{\text{cm}^2}$] is the intensity of the incident radiation, k [$\text{M} \cdot \text{cm}^{-1}$] is absorption coefficient, C [M] is the gas concentration, L [cm] is the length of the optical path, and A (a dimensionless quantity) is absorbance [29]. An alternative, more practical form of the equation is called the Beer–Lambert law. It states that

$$A = k \cdot C \cdot L, \quad (2)$$

where, again, A is absorbance, k is absorption coefficient, L is the length of the optical path and C is concentration [30].

Next, some typically used alternatives of the main components required are reviewed in more detail. Their respective advantages and disadvantages are assessed superficially. Mirrors and optical cuvettes are excluded from the review, as use of mirrors is non-mandatory and as optical & mechanical components are excluded from the scope of this thesis, as explained in section (1.2).

2.3 Infrared radiation emitters

There are many kinds of methods available for producing IR radiation. Most of these methods are suitable to be used for at least some of the IR spectroscopy applications. There are also several manufacturers that produce IR emitter components specifically designed for NDIR applications. IR sources suitable for modern commercial IR spectroscopy devices can be categorized for example by their emission band, which can be

either narrow, or follow the broadband distribution of black-body radiation. According to this division, the methods for producing IR radiation can be treated as *electroluminescent* and *incandescent* sources. When making the decision of which type of an IR radiation source to use in an NDIR sensor, one should take into account at least the following three things: what is the absorption wavelength of the target gas (the source needs to be able to produce radiation at that wavelength band), what is the desired level of detection limit (as it is related to radiation intensity), and what kind of a detector is going to be used.

2.3.1 Electroluminescent sources

The two primarily used electroluminescent IR sources in NDIR applications are IR light-emitting diodes (LED) and semiconductor-based sources utilizing light amplification by stimulated emission of radiation. Research in recent years has produced MWIR-band LEDs that can be used in a variety of industrial gas measurement applications due to the possibility of customizing their emission peak in the manufacturing process [31] and lately many electronics manufacturers have increasingly started to release IR LEDs designed specifically for NDIR applications [32–34]. IR LEDs are very selective as their emission band can be optimized to be suitably narrow, yet wide enough to cover the absorption band of the target substance in its entirety [35]. They consume only a few percent of the power consumption of a typical incandescent source - power consumption for IR LEDs being in the order of milliwatts and for incandescent sources in the order of tens to hundreds of milliwatts. Their long-term stability is good; according to Johnston, a test exceeding 1.5 years of continuous operation showed no mentionable drift in the spectral bandwidth or the output power of an IR LED [36]. IR LEDs have few indisputable objective disadvantages, but a significant one worth a mention is that at wavelengths above 3.3 μm their conductance becomes highly temperature dependent due to a narrow band gap, eventually causing the radiation recombination in the semiconductor to decrease [37]. In other words, single-wavelength standalone IR LEDs cannot operate at the mid-wavelength IR band and above as reliably as at shorter wavelengths. In addition, IR LEDs have many noise sources such as thermal, Poisson, generation recombination, 1/f, and random-telegraph noise [38]. Other disadvantages associated with IR LEDs are mainly of subjective nature and related to the user's requirements for the component; for example, IR LEDs are more expensive than incandescent sources [39] and even though the optical performance of IR LEDs can be considered excellent, it is still not as good as that of semiconductor lasers [40].

Even though IR sources based on lasers can be and are increasingly used in NDIR ap-

plications [6, 41], the branch of spectroscopy utilizing lasers is not exactly NDIR spectroscopy, but more commonly known as laser absorption spectroscopy. Semiconductor lasers, applications of electroluminescence processes [42], offer extremely good optical performance that is superior to that of all the other IR sources available [43]. These top-quality optical properties include their very narrow emission band leading to excellent selectivity, and their high power density that can significantly improve signal-to-noise ratio (SNR). Due to their versatility, lead–salt lasers were for decades the most commonly used type of lasers used in NDIR applications with requirements for a very high precision, down to the parts per trillion level. By modifying the manufacturing process, it is possible to determine their peak emission wavelength from within the range of about 3 to 20 μm (SWIR to the FIR) [44]. The same possibility of choosing the emission wavelength from within even a wider range of 3 to 300 μm applies to the newer technologies like quantum cascade lasers and interband cascade lasers [45]. One major disadvantage of lasers used to be their need of cooling, especially when operating in continuous mode [44]. For some of the laser types, however, the need for cooling can be drastically reduced or even fully bypassed by operating the laser in pulsed mode; in the pulsed operation mode, the laser does not consume power continuously, and thus neither power dissipation, i.e. heat, is continuously generated [45]. In addition, research is constantly being done to further develop lasers that are suitable for NDIR applications and able to operate without cooling [45, 46]. Some commercially available lasers of this type do already exist [47]. The optimal optical performance of lasers comes with a high, often disproportionately expensive unit price - IR sources inferior to lasers can provide good enough performance in many applications. Cost of devices such as laser components is however again a purely subjective type of a drawback arising from the requirements imposed on the device by its user.

2.3.2 Incandescent sources

Incandescent (or *thermal*) IR sources work so that when they heat up due to an electric current flowing through them, they start to emit broadband quasi- or true black body radiation, the emission spectra of which at a few different temperatures can be seen in figure 5 [48]. As can be seen from the figure, the emission peak wavelength and radiant energy of a black body radiator are dependent on the radiation source's temperature. For example, if it would be desired to emit radiation at the MIR band, the radiator temperature should be set to approximately somewhere in between 300 and 1000 K, depending on the exact desired peak wavelength. Before the development of microelectronics manufacturing processes and the large-scale utilization of microtechnology, the most typically used IR source in NDIR applications was an incandescent lamp. Incandescent lamps are inex-

pensive to produce due to their simple manufacturing process. An output energy greater than that of IR LEDs, their wide wavelength range, and affordability are their greatest advantages [49]; in turn they have few but highly impactful disadvantages such as erratic long-term stability that can considerably vary between individual units, and microphonic noise caused by vibration. Regardless of these reliability-impacting disadvantages and although their use is becoming rarer, incandescent lamps are still used as IR sources in NDIR applications [6]. However, better-performing microelectromechanical system (MEMS) based components, like the Vaisala-patented μG , continue to steadily keep on increasing their share in NDIR devices utilizing an incandescent IR source.

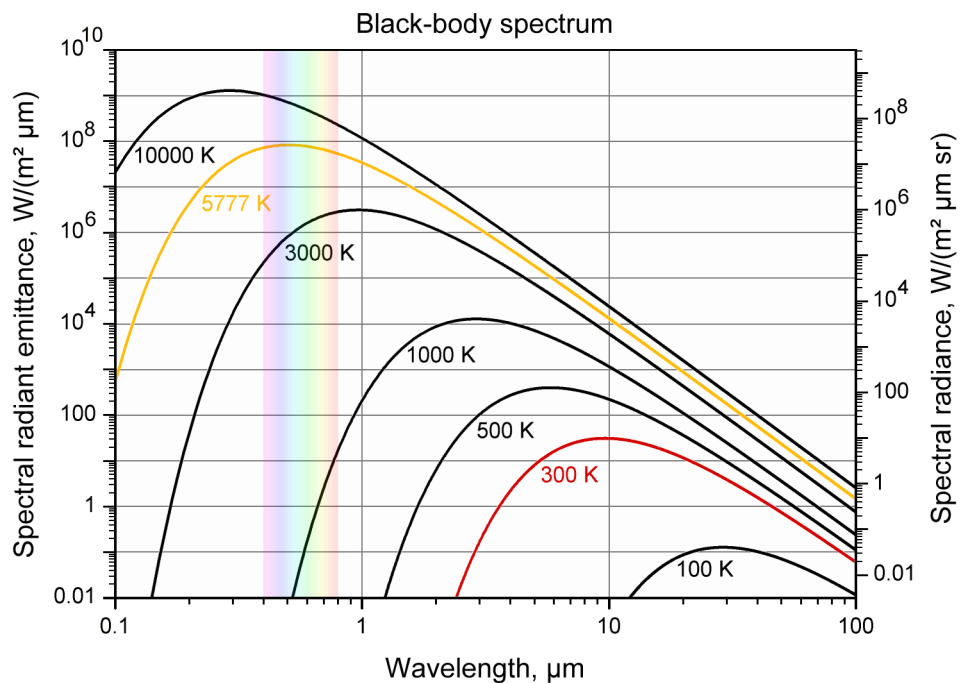


Figure 5. A graph showing black-body radiation distribution at different temperatures on a logarithmic scale. Highlighted are the average temperature of sun (orange curve at 5777 K) and typical room temperature (red curve at 300 K). The figure is retrieved from [48] under the CC BY-SA 3.0 license.

Availability and the number of variations of MEMS-based IR emitters has greatly increased during the last decade and multiple manufacturers now offer extensive product families consisting of emitters designed for different applications. Main differences between the components are related to the size of their active area, power consumption, response time and expected lifetime. Nominal power consumption is typically in the or-

der of hundreds of milliwatts and the response time (time constant) in the order of tens of milliseconds. Lifetime expectancy varies more, from months to as much as several years of continuous operation. Lifetime expectancy is related to the operating temperature; the higher the temperature, the shorter the lifetime expectancy. This, however, is just a generalization - the exact relationship between temperature and life expectancy is more complex and depends, for example, on the materials used in the component. Different packaging/mounting solutions are provided, and usually customer-specific packaging can be arranged. Compared to the incandescent lamp filaments, MEMS-based incandescent emitters can be considered practically rigid as they are very small in size and often built over a silicon substrate. Rigidity of the emitter successfully eliminates the risk of microphonic noise typical for incandescent lamps. MEMS-emitters also offer a significantly better long-term stability, though the actual lifetime expectancy varies a lot between components produced by different manufacturers. [50–53]

Since the basic principle of operation is same for both of the incandescent sources discussed, there are individual negative and positive properties common to both of them. Both incandescent lamps and the MEMS-based emitters can be thought of as thermal components because their operation is based on thermal emission. The time taken for the emitter to warm up and cool makes the response time of incandescent sources to be orders of magnitude slower than that of the IR LEDs and lasers. This makes using them in rapid measurement applications challenging. On the other hand, a common major benefit and a definitive feature for both types of incandescent sources discussed is their broadband, temperature-dependent emission spectrum, which allows them to be used to measure a variety of gases when combined with optical filters. This is a feature that is not an inherent part of the other types of IR sources, like IR LEDs and lasers.

2.4 Optical filters

Optical filters are devices that have a transmittance varying with wavelength. They are based on different operating principles like absorption, acousto-optic effect, refraction, diffraction and interference. Two types of interference-based optical bandpass filters can be used in absorption spectroscopy, where it is important to limit the radiation wavelength to the absorption band of the target gas. Passive monolithic filters, that have a fixed pass-band (or multiple pass-bands), an example of which can be seen in figure 6 (a) and active ones, that have a tunable pass band, as shown in figure 6 (b). Both passive and active interference filters utilize the effects of optical interference and phase shift in order to create a wavelength-dependent passage. There are five main types of passive filters having

a different spectral shape: bandpass filters, notch filters, shortpass edge filters, longpass edge filters and dichroic filters [54]. Passive filters can be implemented, for example, by coating a radiation-transmitting substrate with a layer of anti-reflective coating having a suitable reflection coefficient n and a thickness d equal to quarter of the wavelength λ [55]. In an NDIR sensor, optical filter chips can be placed on top of the emitter, detector, or both of them; sometimes a combination of passive and active filter components is used in high quality measurement devices. Like any other components, also optical filters are non-ideal. Their pass-band transmittance is never 100%, and even though the transmittance of high quality filters can drop very rapidly ($> 90\% / \text{nm}$) at the roll-off region, it is important to note that their transmittance is not 0% everywhere outside the desired pass-band. [56]

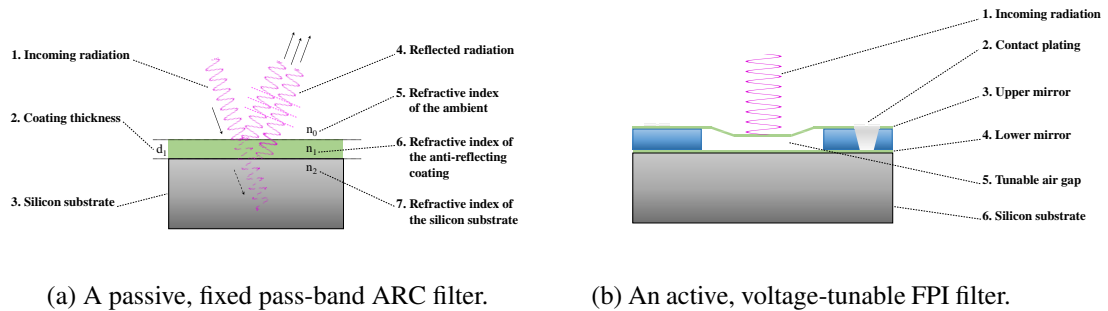


Figure 6. Side-view schematic diagrams of the two different filter types discussed. Subfigure (a) shows a passive filter and subfigure (b) an active filter. For both of the subfigures, main parts of the device as well as other objects of interest are pointed out using dashed lines.

The use of active filters, like the voltage-tunable Fabry–Pérot Interferometer seen in figure 6b, allows measuring both the absorption wavelength of the target gas and a reference wavelength where no absorption occurs, operating at only one optical path using single incandescent IR source and a single detector having a broad enough detectivity. As described in an application note of Vaisala:

"The reference measurement compensates for any potential changes in the infrared source intensity, as well as for dirt accumulation in the optical path, eliminating the need for complicated compensation algorithms. Simple and cost efficient, the single beam dual-wavelength sensor is highly stable over time, requiring minimal maintenance." [57]

2.5 Infrared detectors

As with producing IR radiation, there are also many kinds of methods for detecting it. A commonly used division of IR detectors into two subcategories, consisting of thermal and photonic detectors, is used in this thesis. IR detectors of any type can be enclosed in hermetically sealed component packages, such as the Transistor Outline (TO) cans. The component package can then be filled with an inert gas, like nitrogen, in order to protect the detector chip from environmental factors such as humidity and other contaminants. This can prolong the lifetime of the detector. When choosing the method of detection, it can be wise to begin by first considering the desired spectral response, specific detectivity and response time, as these three key features are characteristic for the different detector types, and are directly related to the detector's suitability for different applications. This kind of an approach can effectively help in limiting the number of detector options to choose from, as these parameters are equally defined for all of the detector types. Other relevant parameters should be considered after choosing the detector type to be used, as these are different for the different types of detectors. An excellent compendium of IR detector figures of merit is included for example in the book "Infrared Detectors" by Rogalski [58]. Therefore, only a brief summary of the main properties is given.

Normalized spectral responsivity describes how sensitive a detector is to different wavelengths [58]. Normalized spectral responsivity is a relative quantity having an arbitrary unit and its values range from 0 to 1 or 0% to 100%. Exact method of calculating the spectral responsivity can vary between detector types - this has to be considered when considering the spectral responsivity of a detector. **Specific detectivity** (or normalized detectivity) D^* [$\text{cmHz}^{1/2}\text{W}^{-1}$, Jones] links together the main characteristics of the detector's performance, i.e. its spectral response, noise equivalent power, and the active surface area of the sensor [58]. The higher the specific detectivity, the better the detector. It should be noted that different noise sources can be dominant for different types of detectors. The **response time** of a detector is determined by the time constant τ . As defined by The International Society for Optics and Photonics: "*The term response time refers to the time it takes the detector current to rise to a value equal to 63.2% of the steady-state value*" [59].

2.5.1 Thermal detectors

The operation of thermal detectors is based on various phenomena caused by a temperature difference or a change in temperature. Thermal detection methods include measuring

a voltage signal generated by means of the thermoelectric effect (thermocouples and thermopiles), observing a change in electrical resistance caused by temperature dependency of the detector (bolometers and microbolometers), measuring the electrical current generated by pyroelectric effect (pyroelectric detectors) and monitoring measurement signal changes caused by thermal expansion of the target gas in a sealed space (Golay cells). Let us break down the main differences of the thermal detector types presented and briefly consider their performance reflecting to the three universal parameters of performance. The spectral response of precisely engineered thermal detectors can be excellently uniform throughout the entire band of IR radiation; however, if an optical window is used to seal the detector housing, the true spectral response is negatively affected by the optical properties of the window. [58]

Figure 7 [60] shows the theoretical specific detectivity of an ideal thermal detector.

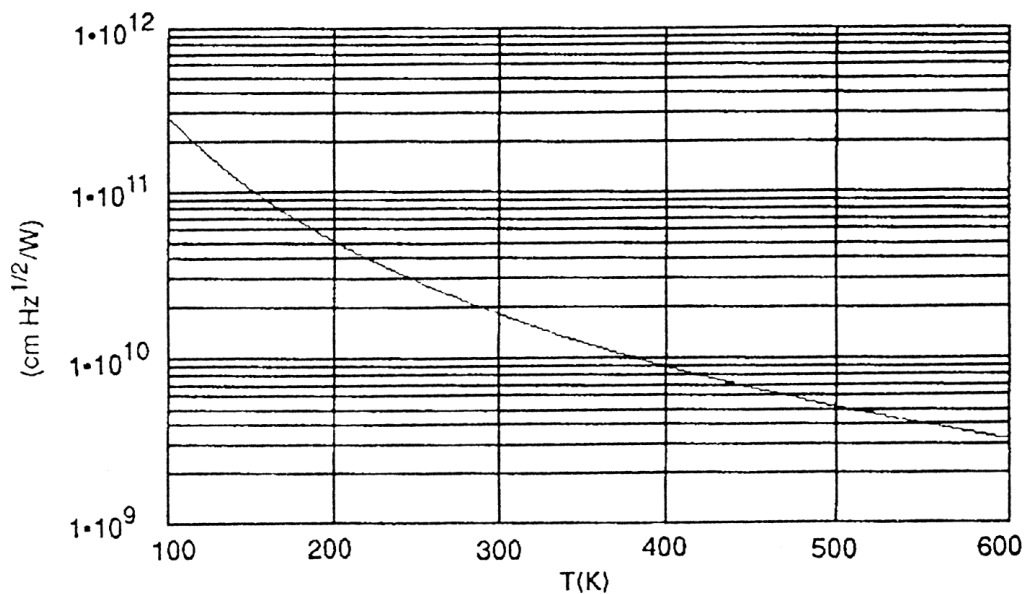


Figure 7. A graph showing the theoretical maximum specific detectivity of a thermal detector on a logarithmic scale as a function of temperature. The figure is retrieved from [60].

When operating at room temperature (295 K) real, non-ideal thermal detectors seldom reach a specific detectivity higher than 10^9 Jones. Out of the discussed types of thermal detectors, commercially available Golay cells, radiation thermocouples and pyroelectric detectors reach the highest detectivity of approximately $7 \cdot 10^8$ to $2 \cdot 10^9$ Jones, while the detectivities of the less sensitive bolometers and thermopiles can typically reach a detectivity of about 10^8 to $2 \cdot 10^8$ Jones [61]. Despite thermopiles being less sensitive than the other types of thermal detectors, they are commonly used in several applications rather than the

more sensitive alternatives because of their excellent reliability and price–performance ratio. As for the response time, thermal detectors are significantly slower compared to photonic detectors due to the slow nature of thermal phenomena, as explained in section (2.3.2). Response time of thermal detectors depends on the detector’s heat capacity and heat loss per second per temperature degree [60]. There is some variance between the τ value of the different types of thermal detectors; typical values of it range from about 1 to 100 ms, which makes using them in applications requiring a short measurement interval unfavorable. For such applications, photonic detectors should be considered. [58]

2.5.2 Photonic detectors

Different types of photonic detectors utilize many kinds of photoeffects, such as photoconductive & photovoltaic effect (photodiodes, p–i–n photodiodes, avalanche photodiodes, etc.), photoelectromagnetic effect (PEM detectors), photo–Dember effect (Dember photodetectors), and photon drag (photon drag detectors). Of these, most research and commercial development work has been done on photonic detectors relying on photovoltaic and photoconductive effects, for which reason they are highlighted in this thesis too. In photovoltaic mode, photons hitting the photodiode’s detection area (depletion region) generate a voltage over the semiconductor’s p–n junction, which in turn creates a measurable photoelectric current. When the p–n junction is connected to an external circuit, such as an amplifier configuration, current will flow through that circuit when the p–n junction absorbs radiation. Alternatively, open-circuit voltage can be measured. Either of these methods enable measuring the amount of radiation reaching the detector. For photovoltaic-mode detection, no bias voltage or a load resistance is required.

When a photodiode is used in photoconductive mode, it could be described as a resistor that is sensitive to radiation. In thermal equilibrium, a semiconductor contains free charge carriers; electrons and holes. The concentration of these charge carriers changes when radiation is absorbed by the semiconductor. If the photon energy of the absorbed radiation is large enough, more free electrons will be generated in the semiconductor material. This increase in free charge carriers causes the conductance of the semiconductor to increase. In photoconductive mode the photodiode is operated under a reverse bias, so the higher electrical current produced by the change in conductance can be observed as a change in voltage drop over a series-connected load resistance. One of the greatest disadvantages of photodiode-based detectors is their material-property-dependent dark current noise, which is defined in [60] as an output current that flows without radiation entering the detector. The effect of dark current, more significant when operating in photoconductive

mode, can be greatly reduced by proper amplifier design and by operating at a lower temperature. [58, 59]

The spectral response of photonic detectors is mainly limited and determined by the material properties of the semiconductors used to fabricate the detector. The wavelength range detectable by photonic detectors designed for NDIR applications sets to between the NIR and MWIR (0.75 to 8 μm) bands of IR radiation, though detectors having their peak detectivity at longer wavelengths do exist. Other factors limiting the spectral response include detector coatings and optical windows, if such are used. The specific detectivity of photonic detectors greatly varies between the different subtypes. Figure 8 [59] shows the specific detectivity of typical commercially available photovoltaic and photoconductive detectors.

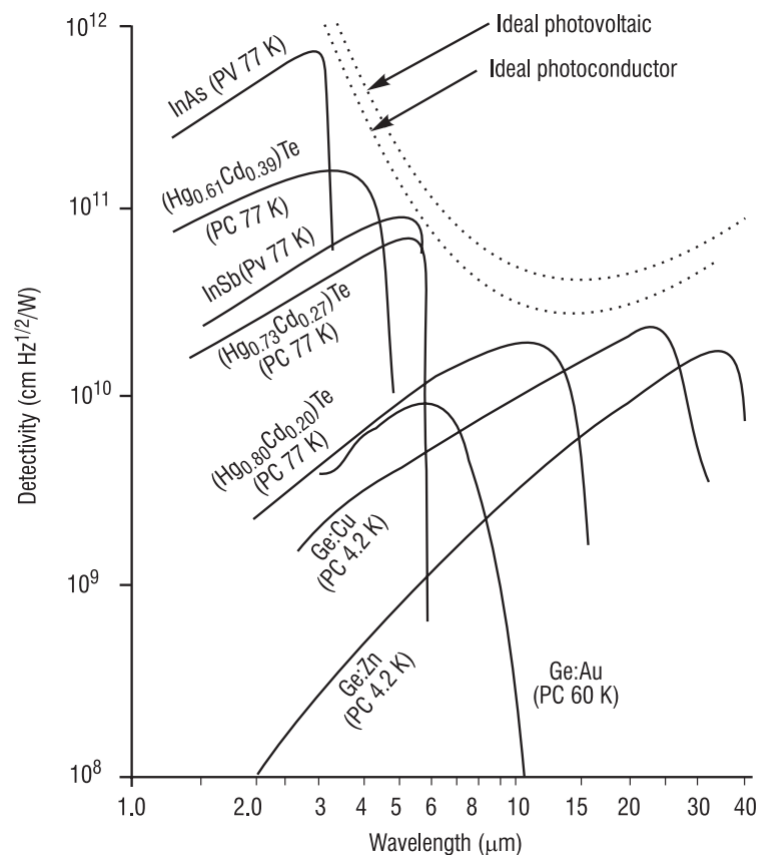


Figure 8. A graph showing typical detectivity of different kinds of cooled photovoltaic (PV) and photoconductive (PC) IR detectors. The graph also includes the ideal detectivity curve for both PV and PC detectors. The figure is retrieved from [59].

As figure 8 [59] implies, certain photovoltaic and photoconductive detectors can reach

a specific detectivity of up to almost 10^{12} Jones, when cooled down to cryogenic temperatures. Even the median value of detectivity for the presented detector types - approximately 10^{10} Jones - is much higher than the typical specific detectivity of thermal detectors. Detectors with high specific detectivity at room temperatures are being studied and further developed - some products are already commercially available. The response time of commercially available photonic detectors ranges approximately from the order of microseconds to the fastest reported response time of in the order of nanoseconds. This makes photon detectors as much as six orders of magnitude faster than thermal detectors. [58, 59]

Until photonic detectors with a high specific detectivity and overall performance at room temperature, such as those reported by Piotrowski and Rogalski in [62] start to emerge on the market on a large scale, various methods can be used to boost the performance of the current-state photonic detectors. For example, thermoelectric cooling can be used to implement a low-power and small-size temperature control system [63]. Cooling the detector and controlling the temperature effectively reduces the chance of random thermal excitation [58] and can thus help to improve performance of the highly temperature-dependent photonic detectors. Detectors that could be used without cooling them would make measuring devices much simpler and thus cheaper and easier to implement. Other methods used to further boost the performance of photonic detectors include adding optical concentrators of various geometries, made of materials that do not interfere with the wavelength range of the detector's spectral response. Typical examples of lens geometries include hemispherical and hyperhemispherical immersion microlenses. These kinds of lenses are placed or formed on top of the detector chip. [64]

In his master's thesis, Huuhtanen theoretically and experimentally compared different methods of IR detection from the perspective of Vaisala's CARBOCAP[®] technology, and concluded that photonic detectors could offer a significant boost in the overall performance of CARBOCAP[®] sensors (including detectivity, SNR and measurement frequency) relative to the thermal detectors included in the comparison [65]. It is therefore well justified to continue the study on the use of photodetectors in the framework of this thesis, as a continuation for the work started by Huuhtanen.

3 ELECTRONICS THEORY

In order to understand practical operation of the electronic components relevant to this thesis and to enable informed and justified component choices to be made, it is necessary to briefly go through the essentially related electronics theory. This chapter examines the basic operating principle of the components with the most significant impact in terms of end result of the design work displayed in this thesis. Essentially related characteristics & parameters and their effect on performance are introduced. In addition, it is briefly assessed which of the available component options and commonly used circuitry associated to them are most suitable for noise-sensitive measurement and instrumentation applications.

3.1 Operational amplifiers

Operational amplifiers (OP-AMP) are electronic devices used for voltage amplification. The most basic form of an OP-AMP consists of two input terminals and a single output terminal. The positive input terminal maintains the phase of the incoming signal while the other, negative one, inverts it by π radians. The output voltage (with a selectable amplification) depends on the voltage difference between the two inputs. In addition to the signal input and output terminals, OP-AMPs naturally also include positive and negative supply voltage terminals. Basic operation and analysis of OP-AMPs is based on the so-called voltage feedback model, a set of idealized assumptions, which describe with sufficient accuracy the operation of the vast majority of OP-AMPs. Basic performance and quality of OP-AMPs is measured by reflecting the actual operation of the device to these ideals. For high-frequency applications (> 1 MHz), current feedback OP-AMPs are preferred. Fundamental parameters describing the operation of OP-AMPs include open-loop gain, closed-loop gain, signal gain, noise gain, loop gain, gain-bandwidth product and phase margin. In noise-sensitive low-frequency applications these parameters are not of concern - the parameters and characteristics relevant to such applications are presented later in this section. Signal & noise gain of an OP-AMP depends on the configuration used. [66]

The two most common configurations used for voltage amplification are the inverting (a) and non-inverting (b) configurations, seen in figure 9.

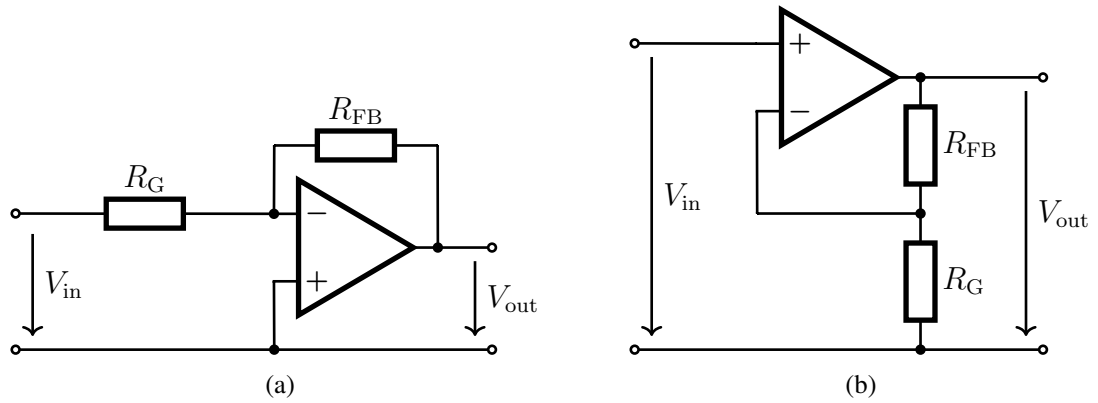


Figure 9. The two basic amplifier configurations of voltage feedback OP-AMPs: (a) inverting OP-AMP and (b) non-Inverting OP-AMP.

The inverting OP-AMP configuration produces an amplified output signal that is, in theory, inverse in phase relative to the input signal. The amplification and output voltage of an inverting OP-AMP are calculated as follows:

$$\begin{cases} A = -\frac{R_{FB}}{R_G} \\ V_{out} = A \cdot V_{in} \end{cases} \quad (3)$$

The corresponding values for a non-inverting OP-AMP configuration are calculated using

$$\begin{cases} A = 1 + \frac{R_{FB}}{R_G} \\ V_{out} = A \cdot V_{in} \end{cases} \quad (4)$$

For both equations (3) and (4) A is gain (or *amplification*) of the amplifier, V_{out} is the output voltage, V_{in} is the input voltage and R_{FB} & R_G are the resistors, whose resistance ratio determines the gain of the amplifier. Worth noting is that both of these configurations also amplify any noise included in the input signal to be amplified. [66]

An amplifying current-to-voltage conversion, necessary for photodiode-based measurement systems, can be implemented by the commonly used transimpedance amplifier (TIA) configuration seen in figure 10.

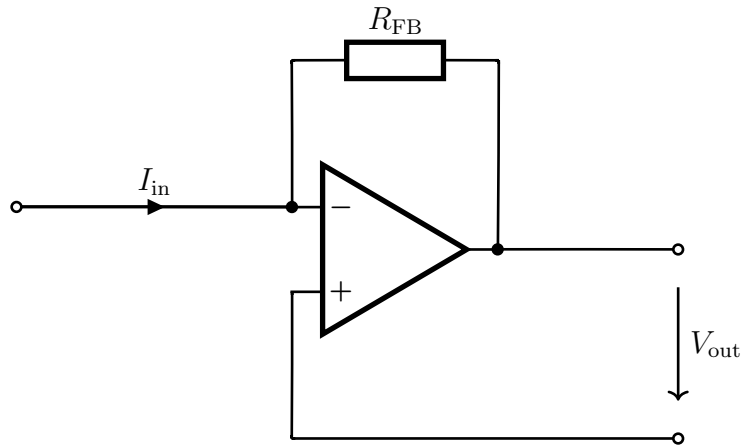


Figure 10. The circuit diagram of a TIA in its simplest form.

Operation of a TIA is based on low input impedance created by negative feedback [67]. When operating at a low frequency, the transimpedance gain is defined by the resistance of the feedback resistor R_{FB} as

$$R_{FB} = \frac{V_{out}}{I_{in}}, \quad (5)$$

where V_{out} is the desired output voltage of the TIA and I_{in} is the input current to be converted into voltage and amplified.

When choosing an OP-AMP for noise-sensitive applications, meaning an application in which any kind of a weak electrical signal in general is subject to amplification, the most crucial parameters to consider include the three internal noise components of OP-AMPs, meaning the differential voltage noise generated across the two input terminals and current noise generated in each of the input terminals. In addition, $1/f$ noise present at low frequencies is a parameter of interest - the lower the $1/f$ noise corner frequency, the better the OP-AMP performance at low frequencies. External noise sources such as resistive and reactive components should be considered too - the contribution of these to the amount of total noise can be limited by reducing the total resistance of the external components used, or by operating at a lower bandwidth [68]. In addition to the noise-related parameters, consideration of other OP-AMP characteristics such as input offset voltage, input bias current, gain, bandwidth and slew rate should not be forgotten [69]. The introduced properties are only those that most significantly affect the overall performance of the amplifier setup; however, for best results *all* of the characteristic parameters and potential

noise sources should be considered when evaluating an OP-AMPs performance in noise-sensitive applications. [66]

In some cases, it can be wise to divide the amplifier setup into two separate stages, resulting in a so-called composite amplifier [70]. This kind of amplifier chaining is well suited for applications where a photodiode is operated [71] and can provide practical design benefits, including at least the possibility of choosing an OP-AMP with good input characteristics as the first stage (preferably a FET input type OP-AMP, unless operating at a high temperature, in which case a bipolar type should be considered [72]), and one with good output characteristics as the second stage. This could possibly even help to save on costs, for conventional OP-AMPs are typically not of good quality in terms of both input and output characteristics.

3.2 Analog-to-digital converters

Analog-to-digital converters (ADC) are electronic components used to convert a time-continuous electrical signal into quantized, discrete format in order to create a defined connection between a physical quantity of interest and its numerical representation. There are many kinds of ADCs available, designed for a wide variety of uses. Nowadays, both high-quality discrete ADCs and those integrated in MCUs, Field-Programmable Gate Arrays, processors and system-on-a-chip devices alike, are available. Hence, it is crucial to understand the basic operating principle of each of the most typical types of ADCs. Main types of ADCs include successive approximation register ADCs, Sigma-Delta ($\Sigma\Delta$) ADCs, and pipeline ADCs. The same basic principles related to choosing electronics of any kind and for any purpose apply to ADCs too. The first things to consider should be the general requirements placed for the A/D conversion by the application, as this helps to delimit the options available. These general requirements include the basic characteristics of ADCs, such as the sampling frequency (samples per second), accuracy (bitrate) and supply power. [73]

For the application of this thesis a moderately low sample rate is enough, as all of the measurements included are related to functionalities with a frequency of way below 100 kHz. This excludes the fastest, pipeline-type ADCs, intended to be used in completely different kind of applications, from the suitable options leaving integrated and discrete successive approximation register ADCs and $\Sigma\Delta$ -ADCs. For the bitrate, 12 bits giving a theoretical maximum of $2^{12} = 4096$ different representable values, is enough. The use of $\Sigma\Delta$ -ADCs having a bitrate higher than 12 bits could be considered, but their price is

disproportionate considering the requirements of the application. Lastly, as the prototype is intended to be powered using USB 2.0, low supply power is a must-have feature. This leaves the options of using either a discrete or integrated successive approximation register ADC, which is well suited for multichannel data acquisition. As an MCU is included in the system implemented as part of this thesis anyway, it should be sensible to consider choosing an MCU with a successive approximation register ADC of sufficient quality; all of the major microcontroller manufacturers do produce such. [73–75]

No matter how high the quality of a measurement system, its performance may be severely degraded by A/D conversion errors. For the highly error-sensitive instrumentation applications specifications for integral nonlinearity error, offset and gain errors, thermal-phenomena related effects, and AC performance should be carefully inspected. In addition, it is highly preferable to estimate the overall system error by performing a measurement uncertainty analysis using either the root-sum-squared method or the worst-case method. [76]

3.3 DC voltage regulators

In electronics it is very often necessary to reduce the main supply voltage for use in the different electrical subsystems. Some subassemblies of the system might run on a different operating voltage than others, or a certain very precise and time-invariant reference voltage may be needed. Such voltage levels - lower than the main supply voltage of the system - can be achieved using a voltage regulator. As there are many kinds of voltage regulators available, the exact method of implementation should be chosen to best match with the requirements of the target subassembly. Because of this, complex electrical systems typically utilize several different ways of voltage regulating.

Resistor voltage dividers are an easy and inexpensive way to create a reference voltage, or to scale a voltage to-be-measured so that it fits within the input range of an ADC. Whenever a more precise reference voltage, less sensitive to possible changes in the operating conditions (like the ambient temperature) is needed, a discrete shunt or series voltage reference should be used. If an output current larger than that of a voltage reference can provide is required, an active voltage regulator should be used. The main types of active voltage regulators include linear regulators and switching regulators. Linear regulators produce less noise and are simpler in terms of circuit configuration, but their efficiency is inferior to that of switching regulators, meaning that they consume a larger amount of power and thus generate a larger amount of heat - however this does not become a

problem if the output current is low. Even though the efficiency of switching regulators is higher than that of linear regulators, meaning that they consume less power and generate a smaller amount of heat, the use of switching regulators should be avoided in noise-sensitive instrumentation applications, as their operation is based on rapid on/off switching and more complex external circuitry - both being factors that inevitably increase the total amount of noise in an electronic system. [77]

3.4 Infrared signal modulation

In theory, if it was possible to exactly define the incident radiation intensity I_0 (see equation 1), an NDIR gas sensor could be realized using DC operating mode. However, in practice it is necessary to modulate the carrier signal at some point of operation. This is because without modulation, the information on the concentration of the target gas (contained in the carrier signal) could not be reliably distinguished from the noise sources affecting the system. Such sources of noise include, for example, ambient IR radiation and different kinds of offset errors (such as photodetector dark current and OP-AMP input offset) that directly affect the measurement. By modulating the IR and using algorithms for processing the measurement data, it is possible to minimize the effect of offset errors to the gas measurement.

AC operating mode can be achieved, for example, by using an optical chopper or by electrically modulating the IR source used. Moving parts typically degrade long-term stability and their miniaturization is rather difficult. For this reason, the latter method, i.e. electrical modulation of the power fed to the IR source, is used in this work. Electrical modulation of the IR source component can be implemented in many ways, for example by using a combination of active components and digital electronics. When modulating the IR source, its response time must be taken into account. Because the IR source used (a Vaisala μG) is of thermal type, it has a somewhat slow response time. This is an inevitable feature of incandescent type sources (as described in more detail in section 2.3.2). The emitter area does not heat up and cool down instantaneously, but instead logarithmically. Thus, when using an incandescent IR source, it is necessary to use a modulation signal with a period longer than the thermal response time of the component. Another possible way to implement AC operating mode is to modulate the tunable optical filter, if such is included in the system. As proposed by Ebermann et al., a faster measurement cycle can be achieved "*by fast switching or sinusoidal modulating the filter wavelength*" [78]. This, of course, requires that a fast enough detector is used, so that modulation of the signal can be observed. As discussed in section 2.5, photodetectors enable the described

faster measurements to be performed, compared to thermal components. Modulation of a voltage-tunable filter can be implemented, for example, by using a digitally controlled switch to alter between any two (or more) operating voltages. Previously performed experiments utilizing the tunable optical filter modulation method, proposed by Ebermann et al. [78], have proven its functionality as well as its significantly fast response time. For this reason, control electronics for modulating the FPI filter are also designed for the prototype implemented as part of this thesis.

3.5 Thermoelectric cooling

Thermoelectric cooling (the operating principle of which is presented in figure 11) is commonly used in many of the photonics-related applications to control the temperature of various kinds of semiconductor components, such as lasers and photodiodes, to readings well below the natural temperature of their operating environment. Thermoelectric cooling is based on the Peltier effect, which describes the transfer of heat energy from a junction to another in a thermocouple, where the junctions are made of materials having unequal Seebeck coefficients. This can be considered as a mechanism opposite to the Seebeck effect, where a temperature difference ΔT creates a voltage difference across the junctions of a thermocouple. In figure 11 the negative and positive charges shifted towards the hot surface represent the charge carrier gradient caused by the voltage across the element, which in turn causes the temperature gradient. [79]

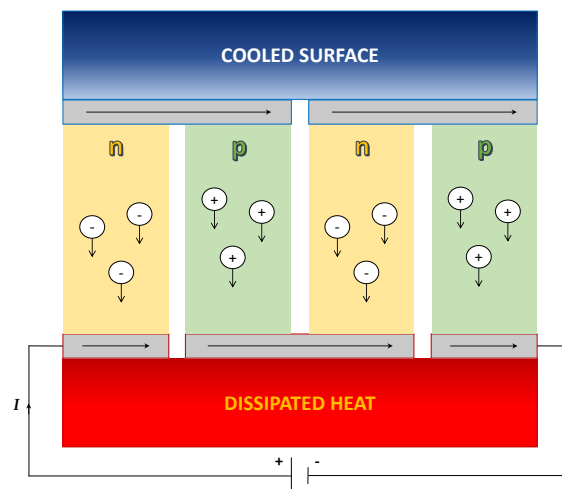


Figure 11. A diagram depicting the Peltier effect being utilized in one of its applications; the thermoelectric cooler. Direction of electric current is represented with black arrows within the electrical conductors colored light-grey.

Some manufacturers produce photonic detectors that are equipped with a thermoelectric cooler (TEC), integrated inside the component package (figure 12 [80]). These integrated TEC modules make it possible to control and keep the temperature of the detector chip, placed atop of the cooler element[s], at a desired value. Multiple TEC elements can be placed on top of each other to achieve a larger maximum temperature difference ΔT_{MAX} between the hot and cold sides of the TEC element. This causes the cooling to be more efficient, as long as adequate heat removal is provided. Typical amount of cooler stages ranges from one to four and typical values of ΔT_{MAX} for the different amounts of stages are approximately as follows: 60 to 72 K for 1-stage setups, 80 to 100 K for 2-stage setups, 100 to 110 K for 3-stage setups, and 110 to 130 K for 4-stage setups. Actual performance is, however, always subject to the ambient conditions. [81]

IR detector

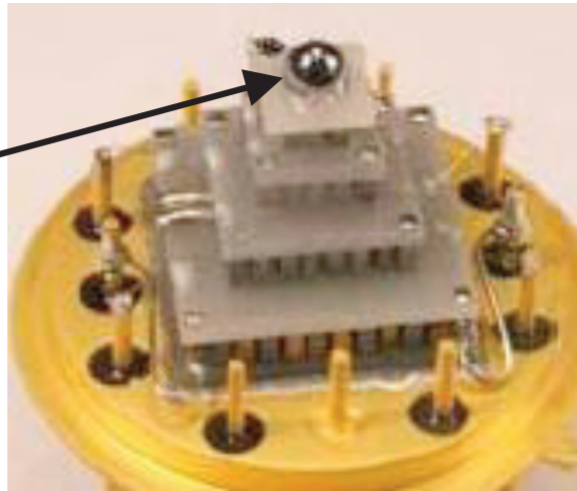


Figure 12. A picture showing an integrated four-stage TEC module, on top of which the IR detector is placed. The figure is retrieved from [80] under the CC-BY-NC-ND-4.0 license.

For the photodetectors with an integrated TEC module it is typical that also a thermistor, located next to the IR detector chip, is included. Thermistors with a negative temperature coefficient (NTC) are more commonly used as they are well-suited for temperature measurement & control applications - thermistors with a positive temperature coefficient exhibit a smaller resistance change over the same temperature range, as well as a characteristic switching point after which the resistance rapidly grows, making them better suited for applications like overcurrent protection and battery charging management [82]. Resistance of a thermistor changes proportionally to its temperature. If an additional, conventional, resistor is introduced to form a voltage divider, the voltage across the voltage-dividing resistor changes proportionally to the temperature, too. Essentially, thermistors

offer a simple and inexpensive way to measure temperature; that information can then be used as a part of a control loop used to maintain a consistent temperature.

3.6 Digital control

Modern measuring instruments are complex embedded systems; mixed-signal devices that use a combination of both analog and digital electronics to enable data acquisition and precise control of the measurement cycle. Typically, a mix of analog and digital electronics has to be used, as the measurement data acquired is analogous in origin, but it is most often desired to be processed and displayed in digital form. These devices also increasingly include Internet of Things capabilities, just like any other commercial electronics nowadays. Microcontrollers can be used to introduce digital control to a system for the purpose of simplifying its operation. Indeed, many of the functionalities that are quite straight-forward to produce by means of digital control design would be more complicated to accomplish using analog electronics only, while some of the functionalities would be completely unreasonable to implement without the use of digital electronics & control. To sum up the potential benefits of digital control, it can significantly increase system flexibility, reliability and programmability in addition to simplifying the system integration and testing processes - all this while reducing design time and largely eliminating the need of discrete tuning components [83].

The most important digital control concepts regarding the application of this thesis include different types of digital control signals and digital control loops. A control signal can be defined as an electrical pulse that represents a software-defined control command [84]. Commonly used control signal types which microcontrollers can typically output are, for example, pulse-width modulated (PWM) square wave and high/low state DC voltages produced by General-Purpose Input/Output pins. PWM can be used for many kinds of purposes, such as controlling the magnitude of instrumentation-related operating voltages, and General-Purpose Input/Output signals for switching various active components such as LED indicators ON and OFF, or for changing the position of a multi-pole digital switch. In connection with this thesis, the need of control is most essentially related to thermoelectric cooling, introduced in section (3.5). A digital Proportional–Integral–Derivative (PID) controller is suitable for the purpose, as demonstrated by Mayursinh et al. [85]. PID controller is a closed-loop control system. It compares the set point value of the controlled parameter (such as temperature) to a measured process variable (such as the linearized voltage of a thermistor corresponding its temperature). In addition to PID, the use of a simpler and slower-reacting PI controller with an easier tuning procedure can

be considered for systems without the need for a fast response - the derivative part of a PID controller makes the system calculate the output using the information of how fast the error term changes, which can cause problems in the form of derivative kicks if noise is introduced to the process variable [86].

4 ELECTRONICS DESIGN

There would be several possible ways to implement the prototype's desired features (described in section 1.2); various technologies and methods are feasible for creating a system that would include at least most of the subsystems and their respective functionalities. Two examples of such feasible technologies would be developing either an Application-specific Integrated Circuit (ASIC), or a system-on-a-chip. However, as Vaisala utilizes a *high-mix low-volume* strategy with an extensive product portfolio and moderate volumes per product type, there is no need to develop highly specialized and complex integrated devices such as ASIC chips. Due to the need for flexibility and since most components used in the products are not purchased in large volumes, the economies of scale would not be achieved, making the design and use of ASICs unnecessarily expensive. These kinds of solutions are indeed better suited for mass production. In addition, the workflow of ASIC chip design process is time-consuming and complicated, making developing an ASIC an inappropriate approach especially in the case of a thesis. For these reasons, and due to the fact that there are many competitive alternatives available among them, discrete components were used in the electronics design of the prototype. The component choices made were mainly based on the theory background presented in Chapter 3. The electronic schematic was designed using PADS[®] Logic, part of a series of electronic computer-aided design software released by *Mentor, a Siemens Business*.

Figure 13 depicts the block diagram introducing all of the main subsystems included in the prototype. As described in section (1.2), the system consists of an MCU, an IR source, a voltage-tunable FPI filter, an IR photodetector & a two-stage amplifier, TEC driver for cooling the detector, as well as the control electronics needed to operate all of these functionalities. In addition to the subsystems presented in the block diagram, the prototype includes operating-voltage related elements and a RS232 serial bus. These subsystems, excluding the serial bus, can be viewed in the circuit diagram figures included in each section of this chapter. Operating voltages are discussed in more detail later on in section (4.7).

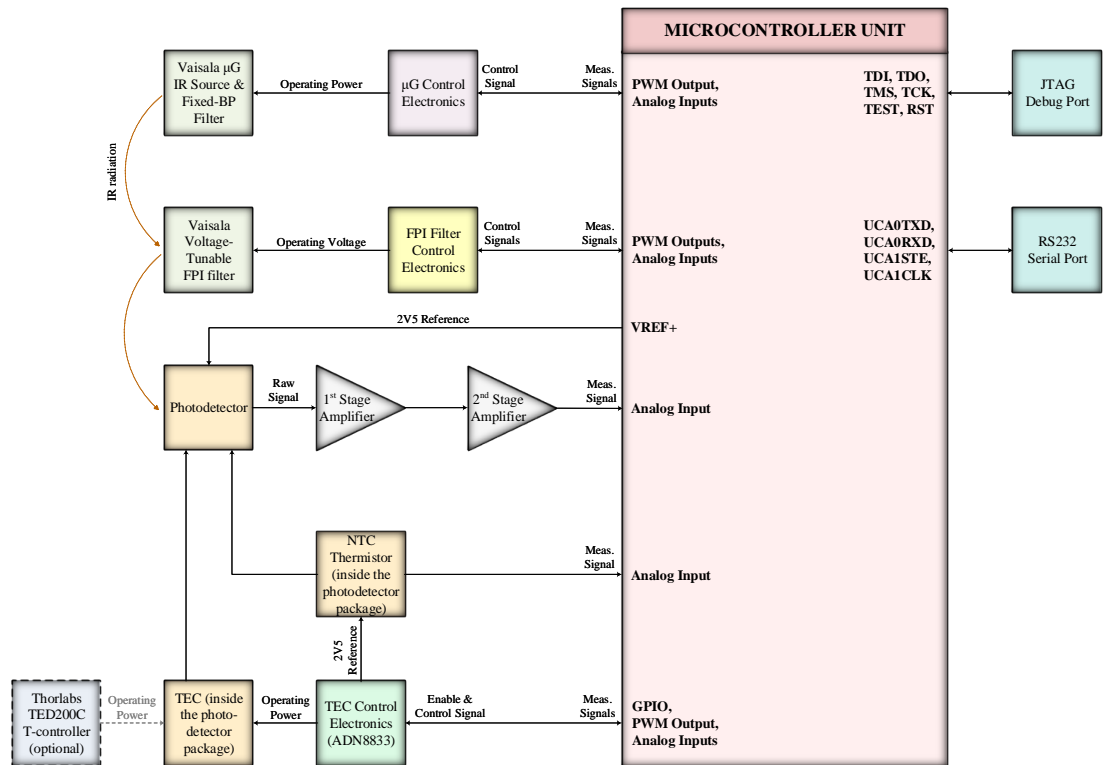


Figure 13. Block diagram of the designed prototype. For the sake of clarity, the block diagram is simplified so that operating voltages of the different subsystems are not shown.

As two detectors, different both by their electrical and mechanical characteristics as introduced further on in section (4.3), were used to test the operation of the prototype, two slightly different design variants were produced. Especially the difference in the mechanical design of the detector packages placed unique requirements for both of the detector types tested.

Notice is hereby given that part of the electrical circuits used and presented in this chapter are designed by other Vaisala engineers. For such subsystems, the original designers of the circuits are referred to either in the captions of the circuit diagram figures, or in the text content describing the subsystem if no figure of the subsystem is presented.

4.1 Passive components

This section presents the justification for the choice of types of general-purpose passive components used, including resistors, capacitors and inductors. The photodetectors chosen, classifiable as passive components depending on the definition used, are considered later on in section (4.3). Resistors, capacitors and inductors were chosen taking into account the different requirements per and within each subsystem including them. Characteristics considered for all of the passive component categories include temperature dependency, noise-related performance, precision and surface-mount device package type. Whenever possible, an attempt was made to favor the use of components that are also used in other electronics designs made by Vaisala. To limit the bill of materials, same passive component values were used as often as possible in the different subsystems.

For passive components within signal paths - such as resistors and capacitors used for amplifier feedback or filtering - components with high precision and low temperature dependency were chosen. As for the component package sizes of the passives; most of them are encased in an imperial 0603 (dimensions $1.55 \times 0.85 \times 0.45$ mm [87]) package or larger, and the prototype contains component packages no smaller than the size of imperial 0402 (dimensions $1.00 \times 0.50 \times 0.35$ mm [87]). There would have been no reason whatsoever to use components smaller than that for early stage prototyping. This is because there were no significant requirements considering the size of the prototype, and because the precision and overall performance of passive components typically decreases with package size. In addition, it was desired that the components could be easily replaced by manual soldering, if needed. Hand soldering components having a package size smaller than 0402 would require excessive expertise and practical experience, as well as vision-enhancing equipment, such as microscopes, to be used to assist in the soldering process.

4.2 Control of infrared source & tunable optical filter

Two separate circuits are used to operate the Vaisala μG IR source and the Vaisala voltage-tunable FPI filter, both located inside the same hermetically sealed 4-lead TO-5 component package. Both of the circuits presented in this section are designed by other Vaisala engineers, but their operation had to be described as they play an important role in the operation of the prototype. The power fed to the Vaisala μG IR source is controlled using a switching metal-oxide-semiconductor field-effect transistor operated with an ampli-

fied, low-pass filtered, PWM control signal. Voltage over the μG and the current flowing through it are measured to get information of the amount of power consumed. The control electronics used to operate the μG IR source are designed by Senior Electronics Engineer Niskanen A. of Vaisala.

Circuit diagram of the FPI filter control circuit can be seen in figure 14. The Analog Devices ADG839 (A7), a single-pole double-throw switch, is used to modulate the FPI filter between any two voltages within the range of 0 to 30 V in order to alter the pass-band of the filter between selected wavelength bands corresponding the two operating voltages chosen. The position of the switch (A7) is controlled using one of the General Purpose Input/Output pins of the MCU.

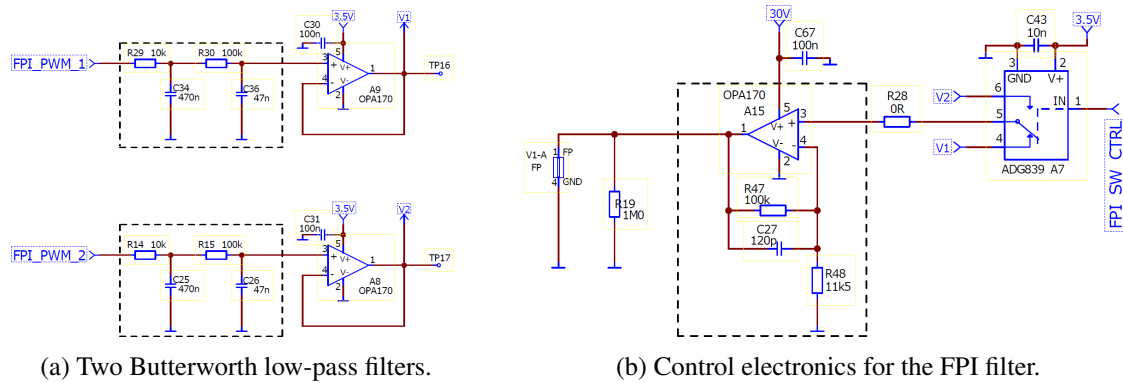


Figure 14. (a) shows the active low-pass filters used to produce the two operating voltages for the FPI filter and (b) is the electronic schematic of the FPI filter control electronics. Both of these circuits are designed by Research Scientist Huuhtanen M. of Vaisala.

In the subfigures (a) & (b) of figure 14, reference designators V1 & V2 represent the two voltage levels used to drive the FPI filter's pass-band to different wavelength bands. Capacitors C30, C31, C43, C67 are used to filter electronic noise.

4.3 Infrared photodetectors

Two photovoltaic detector samples were alternately used to test the operation of the prototype: a VIGO System PVIA-2TE-5 and a Hamamatsu Photonics P13243-222MS. They are presented in this section, limiting the review to the basic features and electrical properties of them, as well as the mechanical properties of the component housing (specific to both of the detectors tested).

The detectors are mounted to the PCBs using pin receptacles manufactured by Mill-Max (mfr. part no. 4015-0-43-80-30-27-10-0). The use of pin receptacles allows the components to be easily attached and detached without soldering, which could potentially damage the detectors as they are sensitive to high temperatures. These particular pin receptacles were chosen as they take up only a very small area of the circuit board and match with the cross-sectional area of the component leads of both of the detector types tested. The number of pin sockets added to the design matches the number of component leads used. In other words, sockets are not added for unused leads of the component packages for this would incur unnecessary costs. In addition to mounting the detectors, the same pin receptacles are used to mount the TO-5 package housing the Vaisala IR source & FPI filter, discussed in section (4.2), too.

4.3.1 Detector type 1: VIGO System PVIA-2TE- λ_{opt}

The VIGO System PVIA-2TE- λ_{opt} is a product family of photovoltaic IR detectors with an integrated 2-stage TEC element, and an optional hyperhemispherical (or hemispherical) immersion lens which is used to boost the optical gain of the detector to improve its SNR. Also included inside the package is a set of water absorbers, that prevent condensation of water vapor in the case of rapid temperature changes. Most of the properties are customizable upon customer request; for example it is possible to choose an optical window with a wedged profile, meaning that the upper surface of the window is non-perpendicular to the angle of incidence of the incoming radiation. This feature helps to prevent direct backscatter which can cause changes in performance, or even optics damage in applications utilizing a high-power source like a laser. The λ_{opt} in the detector product code denotes the optimal wavelength (i.e. the wavelength with highest minimum guaranteed D^*) in μm - versions ranging from an optimized wavelength of 3 μm to 10.6 μm are available as standard. Other characteristics presented in the datasheet include D^* for λ_{peak} and λ_{opt} , current responsivity length product $R_i \cdot L$ at λ_{opt} [$\frac{\text{A} \cdot \text{mm}}{\text{W}}$], time constant τ [ns], and resistance optical area product $R \cdot A$ [$\Omega \cdot \text{cm}^2$]. [88]

PVA-2TE-5AR (figure 15) was selected as the 1st detector alternative for testing the prototype designed. The variant chosen features an optical area of 0.10×0.10 mm and a field of view of 70° with no immersion. The component package chosen is a hermetically sealed 12-pin straight-edged TO-8 with a threaded fastening bolt located at the middle of the bottom surface. The bolt can be used to attach a heat sink when the integrated TEC element is used, more of which later on in section (4.5.4). The TO-8 package is sealed using a wedged window made of anti-reflection coated aluminum oxide (Al_2O_3). [88]



Figure 15. A photograph of the detector type 1: VIGO System PVIA-2TE-5.

The integrated 2-stage TEC element is capable of cooling the detector down to a temperature of approximately 230 K in favorable operating conditions, noting that the declared ΔT_{\max} of the device is 92 K. Maximum values for the operating voltage and current are 1.3 V and 1.2 A, respectively. This gives the theoretical maximum cooling capacity Q_{\max} of 360 mW. A Murata NCP03XM222E05RL NTC thermistor is placed on top of the TEC element, next to the detector chip, to allow temperature monitoring and implementation of a temperature control system. To improve the performance of the integrated TEC, as well as to protect the detector chip from harmful contaminants as described in section (2.5), the component package is filled with a mixture of dry noble gases with low thermal conductivity. [88]

4.3.2 Detector type 2: Hamamatsu Photonics P13243

The Hamamatsu Photonics P13243 is a series of photovoltaic detectors designed for gas detection, radiation thermometer and flame detection applications. The series features detectors with high sensitivity and a fast response. Variants both with and without a TEC element (having a maximum amount of four stages) are available. As standard, two different optical window materials - silicon with anti-reflecting coating, and pure sapphire - are available. Hamamatsu Photonics offers the possibility of customizing the component package as well as the optical filters and lenses used. The spectral response is optimized

over the range of between about 2 to 5 μm slightly depending between the variants available, however peak detectivity should occur at 4.1 μm regardless of the version. The main optical and electrical characteristics declared in the datasheet include D^* for the peak sensitivity wavelength λ_p , photosensitivity S at λ_p [mA/W , V/W], minimum and typical shunt resistance R_{sh} [$\text{k}\Omega$], typical and maximum noise equivalent power NEP at λ_p [$\text{W}/\sqrt{\text{Hz}}$] and typical rise time t_r [ns]. [89]

P13243-222MS (figure 16) was selected as the 2nd detector alternative for testing the prototype designed. It has a photosensitive area of $0.70 \times 0.70 \text{ mm}$ and a field of view of 113° . The package solution chosen is a conventional 6-pin TO-8 with a brim wider than the main mechanical body, located at the junction of the package cap and bottom. The optical window enclosing the TO-8 package is made of sapphire. [89]



Figure 16. A photograph of the detector type 2: Hamamatsu Photonics P13243-222MS.

The ratings given for the integrated 2-stage TEC element are as follows. In ideal conditions the temperature difference between the cool and hot surfaces can reach 70 K. In a typical room temperature of 298 K, the lowest reachable element temperature is 243 K, with a ΔT_{max} of 55 K. The TEC element should be operated at most with 1 V maximum voltage and 1 A maximum current, and a heat sink with a thermal resistance of 3 $^\circ\text{C}/\text{W}$ is recommended. A built-in NTC thermistor (with specifications given in [89]) is included and located atop the TEC element and close to the detector chip, to allow for implementation of a temperature control system. [72]

4.4 Photodetector signal amplification

As photovoltaic-mode photodetectors produce only a very weak current signal and it was desired that the measurement signal would be eventually converted into digital format using an ADC, an amplifying current-to-voltage conversion was required. A chained two-stage OP-AMP configuration consisting of a TIA followed by an inverting OP-AMP circuit is used for the purpose.

4.4.1 Stage 1: transimpedance amplifier

The current signal produced by the IR photodetector (4.3) is first amplified and converted into a voltage signal. Analog Devices LTC2057 was chosen as the OP-AMP of the 1st stage (figure 17). It is a low-noise, zero-drift precision OP-AMP designed for measurement and instrumentation systems, with proposed applications ranging from low-side current sensing to high resolution data acquisition. The component meets most of the essential requirements, such as input-performance related criteria, set out in the theoretical background section (3.1) discussing OP-AMPs. [90]

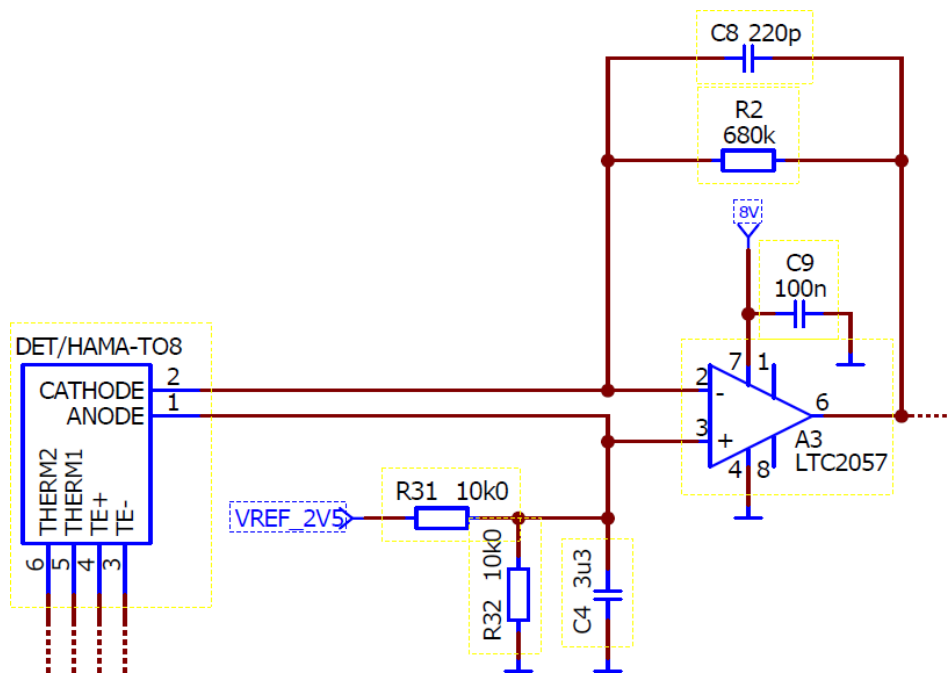


Figure 17. A screenshot of the electronic schematic, showing the 1st stage of the amplifier setup. Signal paths marked with dashed lines indicate that the circuit continues outside the figure.

The positive input terminal of the OP-AMP is provided with a reference voltage of 1.25 V, created using a high-precision resistor voltage divider, in order to operate within the dynamic range of the ADC. Other component values for the TIA configuration were selected based on the Texas Instruments application note SLAA926A [91]. First, the resistance of the gain resistor (R_2 in figure 17) was set by equation

$$R_2 = \frac{V_{oMax} - V_{oMin}}{I_{iMax}}, \quad (6)$$

where V_{oMax} is the desired maximum output voltage, V_{oMin} is the desired minimum output voltage, and I_{iMax} is the maximum input current.

The maximum output and input voltages were selected taking into account the input range of (and the reference voltage set for) the ADC used. The maximum and minimum output voltages V_{oMax} and V_{oMin} were initially set to 1.75 V and 0.75 V, respectively. For the maximum input current I_{iMax} , a much-underestimated initial guess of 1.5 μ A was chosen. Consequently, the resistance of the gain resistor was initially set to 680 k Ω . The selected feedback resistor is 0603 (imperial) in size and could thus be easily changed by hand in case the magnitude of the gain needs to be altered. It should be noted that as the shunt/series resistance of the detector types 1 and 2 is different, a different 1st stage feedback resistance value should be used for the detectors for optimal performance. This is because if the feedback resistance exceeds the detector's shunt resistance, the input noise & offset voltages of the OP-AMP will be multiplied by $1 + \frac{R_f}{R_{sh}}$, causing degraded performance [72]. However, to simplify fabrication, each circuit board is initially furnished with the same resistors. From the point of view of SNR the value of the feedback resistance is insignificant, as both the signal and all the noise terms are equally amplified. The feedback capacitor (C_8 in figure 17) should be chosen so that it meets with the circuit bandwidth, using equation

$$C_8 \leq \frac{1}{2 \cdot \pi \cdot R_2 \cdot f_p} \leq 1600 \text{ pF}, \quad (7)$$

where R_2 is the resistance calculated using equation (6) and f_p is the closed-loop bandwidth. A capacitor with the nominal value of 220 pF was chosen as the feedback capacitor C_8 in order to form a passive low-pass RC filter together with resistor R_2 , having a cutoff frequency of approximately 1 kHz. As the application is not high-frequency in terms of the signals present in the system and the electronics used (the prototype operates below the frequency of 100 kHz), the adequacy of the OP-AMP gain bandwidth should not cause

any concern. Lastly, since the TIA configuration is based on creating a low-impedance input, a similar kind of low-impedance operating point is also required at the node combining the anode of the photodetector, R31, and R32 to the non-inverting input terminal of the first stage OP-AMP A3. This was accomplished by placing C4, a 3.3 μF capacitor, in between that node and the analog ground. Capacitor C9 is used to filter high-frequency noise off the supply voltage of A3.

4.4.2 Stage 2: inverting amplifier

After the current-voltage conversion, the measurement signal of the photodetector has to be further amplified (or *scaled*) in order to make it efficiently readable by the ADC of the MCU (4.6). The 2nd stage (figure 18) is implemented using a conventional inverting OP-AMP configuration, and it utilizes a Texas Instruments OPA180 which is a near zero-drift, high-precision OP-AMP with a close to rail-to-rail output swing.

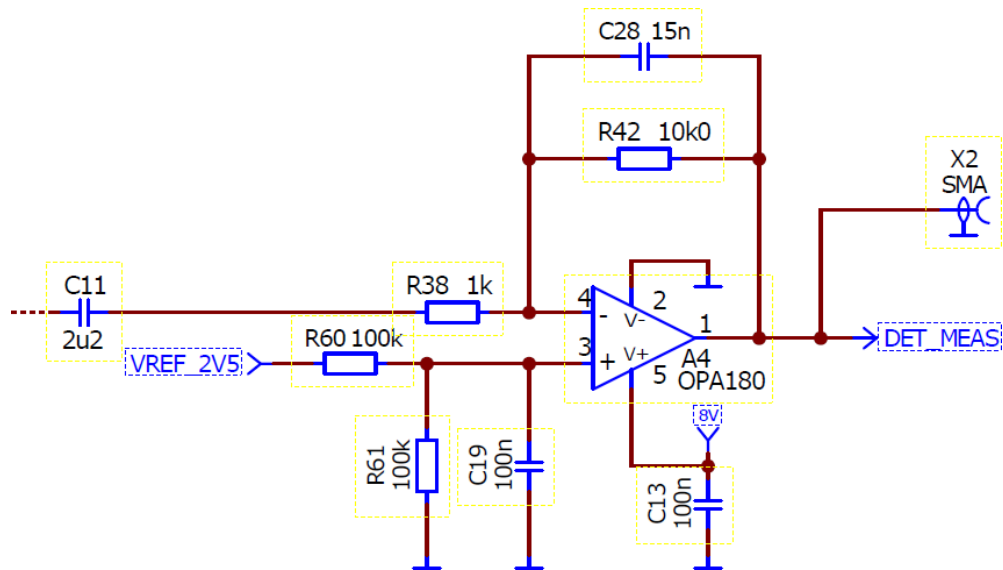


Figure 18. A screenshot of the electronic schematic, showing the 2nd stage of the amplifier setup. Signal paths marked with dashed lines indicate that the circuit continues outside the figure.

Before the measurement signal enters the 2nd stage of the amplifier, the DC component of the signal is decoupled using C11, a 2.2 μF capacitor. This capacitor together with R38 also forms a passive high-pass RC filter with a cutoff frequency of approximately 70 Hz. Again, the positive input terminal of the OP-AMP is provided with a reference voltage of 1.25 V, similarly to the 1st stage. The gain of the 2nd stage was initially set

to 10 by resistors R42 and R38, using equation (3). As with the 1st stage, a passive low-pass filter having a cutoff frequency of about 1 kHz was realized by connecting a 15 nF feedback capacitor C28, parallel to the feedback resistor R42. Capacitor C13 is used to filter high-frequency noise off the supply voltage of A4, and connector X2 is a horizontal PCB-mounted *SubMiniature version A* type coaxial connector that makes it possible to easily observe the waveform of the amplified photodetector signal using an oscilloscope. Lastly, reference designator DET_MEAS carries the measurement signal to an analog input of the MCU.

4.4.3 Design verification by simulation

The simplified operation of the amplifier setup was simulated using LTspice[®], an open-source electronic circuit Simulation Program with Integrated Circuit Emphasis originally released by Linear Technology Corporation, part of Analog Devices from March 2017 onwards. In the simulation performed, both of the amplification stages were combined to form the full 2-stage amplifier setup. The simulation was done using models provided by the manufacturers of the OP-AMPS used. Equivalent circuits of the photodetectors used were not created as some of the required parameters were unavailable. Instead, the current produced by the photodetector was simulated ignoring any non-idealities, using a sinusoidal current source with a peak-to-peak current value of 50 nA as the test signal. Output of the simulation performed can be seen in figure 19.

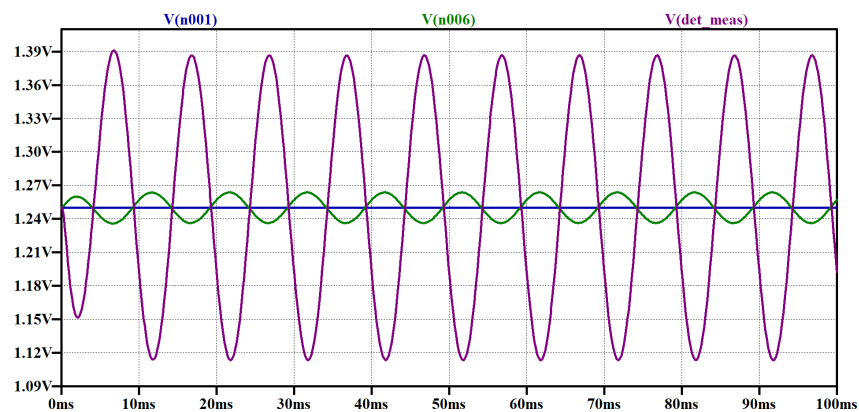


Figure 19. The simulated photodetector signal before (blue) and after the 1st (green) and the 2nd (purple) amplification stages.

The simulation performed was highly idealized and simplified, and was done to examine

merely the fundamental operation of the designed amplifier circuit. It should be noted that the simulation did not consider many of the aspects crucially related to amplifier design.

4.5 Detector temperature control

As a novel feature, detector temperature control electronics were designed. The temperature control system (figure 20) used to control the temperature of the detector's integrated TEC element was implemented using ADN8833, a monolithic ultracompact high-efficiency TEC controller manufactured by Analog Devices, Inc. [92]. ADN8833 is the software-controlled variant of the ADN883X family, subcategory of the Analog Devices *TEC Controller* product category. The controller is operated with a digital control loop. It should be sensible to choose the software-oriented variant of the device as an MCU (presented in section 4.6) capable of controlling it is included in the prototype. In addition, choosing a relatively recently released single-chip solution developed by a large-scale manufacturer should also support possible future productization of the device, as the long-term availability is likely better secured compared to the small-scale manufacturers offering similar kinds of solutions.

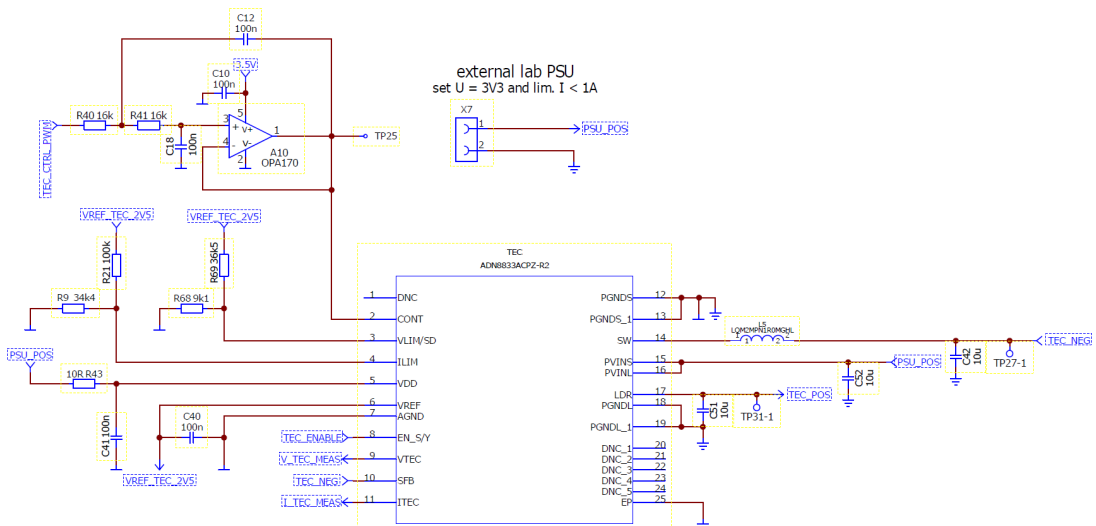


Figure 20. A screenshot showing the electronic schematic of the TEC temperature control circuit. In addition to the ADN8833 TEC driver and the passive components needed to operate it, the circuit includes active filtering of the control signal and a screw terminal input for an external power supply.

The functionalities of the ADN8833 include a patented single-inductor architecture, TEC

voltage and current monitoring, possibility of setting the maximum voltage and current used for cooling, as well as a 2.50 ± 0.025 V reference output. Chapters *Theory of Operation* and *Applications Information* of the ADN8833 datasheet were used as a basis for the electronics design associated with the component. [92]

Selection of the passive components related to the driver's input and output, as well as general electromagnetic interference filtering (including inductor L5 and capacitors C40, C41, C42, C51 and C52), was done according to the application information provided in the ADN8833 datasheet [92]. Test points TP27-1 and TP31-1 are plated through-holes that allow conducting the TEC driver's output off the circuit board with wires soldered to the test points - this feature was used during development of the associated digital control loop, and for experimentally testing the operation of the controller.

4.5.1 General setup

The desired limit of the maximum TEC voltage was set by a resistor voltage divider using the following equations:

$$V_{\text{TEC_MAX_COOLING}} = V_{\text{VLIM_COOLING}} \cdot A_{\text{VLIM}}, \quad (8)$$

where $V_{\text{TEC_MAX_COOLING}}$ is the desired voltage limit of 1.0 V and $A_{\text{VLIM}} = 2$ V/V. From equation (8) it was then solved that $V_{\text{VLIM_COOLING}} = 0.5$ V. [92]

$$V_{\text{VLIM_COOLING}} = \frac{V_{\text{REF}} \cdot R_{\text{R68}}}{(R_{\text{R69}} + R_{\text{R68}})}, \quad (9)$$

where $V_{\text{VLIM_COOLING}}$ is 0.5 V as calculated using equation (8), V_{REF} is the ADN8833's internal reference voltage of 2.5 V, and R_{R69} is a preselected resistance value of 36.5 k Ω . With these parameters, the required resistance R_{R68} was solved; its value should be approximately 9.1 k Ω . [92]

The maximum TEC current limit was set starting from the following equation:

$$I_{\text{TEC_MAX_COOLING}} = \frac{V_{\text{ILIMC}} - 1.25 \text{ V}}{R_{\text{CS}}}, \quad (10)$$

where $I_{\text{TEC_MAX_COOLING}}$ is the preferred TEC current limit of 0.8 A given in the application notes for the sample detectors 1 & 2 [72, 93], and R_{CS} is the TEC driver's internal current sink resistance of 0.285 V/A. The value of V_{ILIMC} could then be solved; it is equal to 1.67 V. [92]

Then, by combining equations

$$\begin{cases} V_{\text{ILIMC}} = V_{\text{ILIMH}} + I_{\text{SINK_ILIM}} \cdot \left(\frac{R_{\text{R21}} \cdot R_{\text{R9}}}{R_{\text{R21}} + R_{\text{R9}}} \right) \\ V_{\text{ILIMH}} = V_{\text{REF}} \cdot \frac{R_{\text{R9}}}{R_{\text{R21}} + R_{\text{R9}}} \end{cases} \quad (11)$$

a simplified form was obtained:

$$V_{\text{ILIMC}} = \frac{V_{\text{REF}} \cdot R_{\text{R9}}}{R_{\text{R21}} + R_{\text{R9}}} + I_{\text{SINK_ILIM}} \cdot \left(\frac{R_{\text{R21}} \cdot R_{\text{R9}}}{R_{\text{R21}} + R_{\text{R9}}} \right), \quad (12)$$

where V_{REF} is the ADN8833's internal reference voltage of 2.5 V, R_{R21} is a generic resistance value 100 k Ω selected for R21, and $I_{\text{SINK_ILIM}}$ is the 40 μA current drawn by the internal current sink of the ADN8833. Finally, the suitable resistance value R_{R9} for the second resistor R9 (part of the voltage divider defining the maximum TEC current in cooling mode) could be solved; it should be approximately 34.4 k Ω . [92]

For easy monitoring of the actual voltage over the TEC and the current flowing through it, the ADN8833 includes analog outputs VTEC and ITEC with voltages proportional to their corresponding quantities. Equations used to convert the voltages of VTEC and ITEC into the actual voltage across the TEC and the actual current flowing through it are

$$\begin{cases} (V_{\text{LDR}} - V_{\text{SFB}}) = \frac{V_{\text{VTEC}} - 1.25}{0.25} \\ I_{\text{LDR}} = \frac{V_{\text{ITEC}} - 1.25}{R_{\text{CS}}} \end{cases} \quad (13)$$

where the subtraction of the linear driver output voltage and the PWM TEC driver output ($V_{\text{LDR}} - V_{\text{SFB}}$) equals to the voltage over the TEC, I_{LDR} is the current output of the linear driver (i.e. the current flowing through the TEC), and R_{CS} is the current sense gain of 0.525 V/A. A voltage of 1.25 V on the VTEC and ITEC pins corresponds to a situation where the voltage across the TEC is 0 V and the current flowing through it is 0 A. [92]

4.5.2 Thermistor linearization

Temperature of the thermistors located on top of the TEC elements of detectors 1 & 2 is used as the process variable of the control loop. The nonlinear voltage response of the NTC thermistors was linearized by hardware, as a linearized voltage response enables better accuracy for the temperature measurement. Two alternative hardware-based methods for thermistor linearization, both of voltage-mode type, were compared by simulating them using LTspice[®]. The one performing theoretically better was chosen and implemented. The comparison was done separately for both of the sample detector types, as they contain different kinds of NTC thermistors having differing thermal responses. Finally, a polynomial fit was created for both of the linearization models designed, using MATLAB[®]. The polynomial fit makes it possible to estimate the detector's temperature based on the linearized voltage of the thermistor read by an analog input of the MCU.

Linearization method 1. (proposed in the ADN8833 datasheet [92]) utilizes two additional linearization resistors R_x and R , connected in series with the thermistor, as seen in figure 21. Their values can be set using equations

$$\begin{cases} R_x = \frac{R_{\text{LOW}} \cdot R_{\text{MID}} + R_{\text{MID}} \cdot R_{\text{HIGH}} - 2 \cdot R_{\text{LOW}} \cdot R_{\text{HIGH}}}{R_{\text{LOW}} + R_{\text{HIGH}} - 2 \cdot R_{\text{MID}}} \\ R = R_x + R_{\text{TH_AT_25}^\circ\text{C}} \end{cases} \quad (14)$$

where R_{LOW} is the thermistor's resistance at the lowest operating temperature, R_{MID} at the median temperature, R_{HIGH} at the highest temperature, and $R_{\text{TH_AT_25}^\circ\text{C}}$ is the thermistor's resistance at room temperature, namely 25 °C.

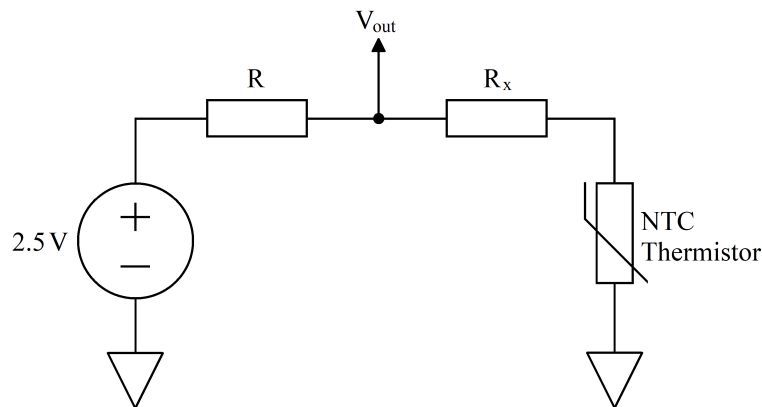


Figure 21. The electronic schematic of the simulated method 1. linearization circuit.

Two different combinations of resistances R_x and R , calculated using equation (14) and rounded to the nearest genuine resistor values, were simulated. The resistor combinations simulated are listed in Table 2.

Table 2. Resistance value combinations used to simulate linearization method 1.

Combination	R_x (Hamamatsu / VIGO)	R (Hamamatsu / VIGO)
1	19.3 k Ω / 6.57 k Ω	43.7 k Ω / 14.5 k Ω (R_{th} at 25 °C)
2	19.3 k Ω / 6.57 k Ω	28.4 k Ω / 8.75 k Ω (R_{th} at 0 °C)

Linearization method 2. (proposed in the Texas Instruments Application Report SNOAA12 [94]) utilizes two additional linearization resistors as well, but in a different configuration seen in figure 22. The first resistor R_s is connected in series with the parallel connection of the second resistor R_p and the thermistor.

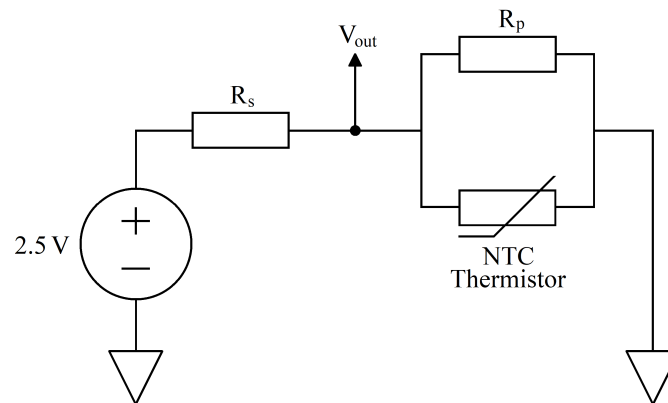


Figure 22. The electronic schematic of the simulated method 2. linearization circuit.

Two different combinations of resistances R_s and R_p were simulated; the resistor combinations simulated are listed in Table 3.

Table 3. Resistance value combinations used to simulate linearization method 1.

Combination	R_s (Hamamatsu / VIGO)	R_p (Hamamatsu / VIGO)
1	12.1 k Ω / 4.00 k Ω	24.3 k Ω / 8.00 k Ω (R_{th} at -5 °C)
2	10.7 k Ω / 3.28 k Ω	19.3 k Ω / 6.55 k Ω (R_{th} , full T-range)

Next, the results of the linearization method comparison are presented. Figure 23 shows the simulated linearized voltage response over the temperature operating range of the Hamamatsu thermistor.

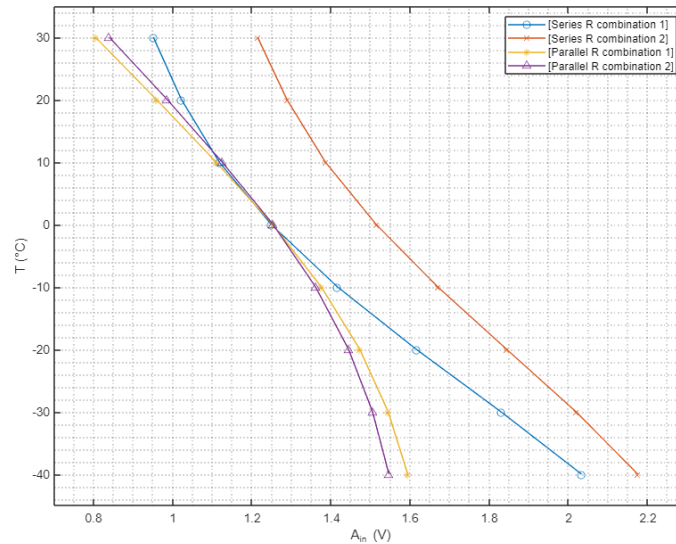


Figure 23. The simulated linearized voltage responses of methods 1 & 2 for the Hamamatsu thermistor over the temperature range of -40 to +40 °C.

Figure 24 shows the simulated linearized voltage response over the temperature operating range of the VIGO (Murata) thermistor.

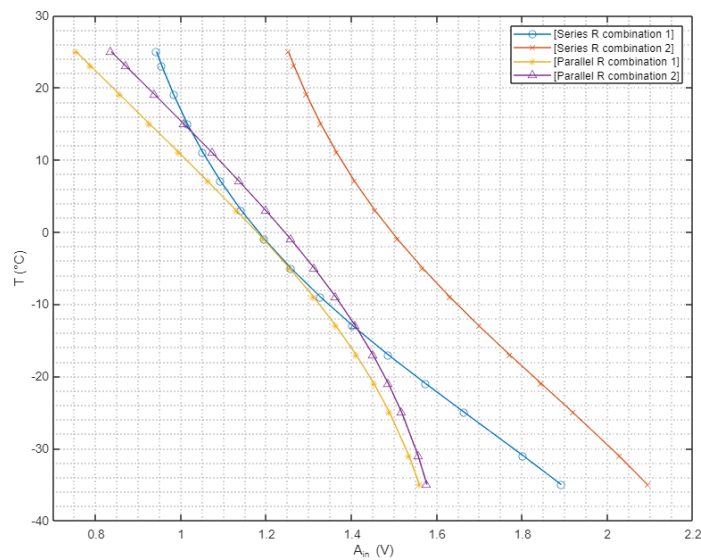


Figure 24. The simulated linearized voltage responses of linearization methods 1 & 2 for the VIGO (Murata) thermistor over the temperature range of -35 to +25 °C.

As seen in figures 23 and 24, linearization method 1. with resistance combination 1 gives the steepest slope for the output voltages between the temperature end points; 0.95 V to 2.05 V for the Hamamatsu thermistor, and 0.95 V to 1.9 V for the VIGO (Murata) thermistor. This means that largest portion of the ADC's input range is utilized. In addition, highest linearity over the low end of the temperature range is achieved. Results of the comparison performed thus show that linearization method 1. should work best for the thermistors of both detectors - hence, method 1. with the better-performing resistance combination was chosen and implemented. The temperature of the thermistor can then be easily calculated by measuring V_{out} of figure 21 and using an n^{th} degree polynomial curve fitting by saving the fitted polynomial coefficients in the MCU's ferroelectric semiconductor random-access memory. Another way of implementing the temperature estimation would have been utilizing the Steinhart–Hart equation. The equation contains a natural logarithmic operation and using it would thus have required excessive computing power or storing a large lookup table of over 60,000 entries (instead of the few polynomial coefficients) in the memory of the MCU, making the implementation unnecessarily complex.

4.5.3 Control signal filter

The digital temperature control loop is closed by feeding a DC control signal to the CONT pin of the ADN8833. As the MCU used (4.6) does not include an integrated Digital-to-Analog Converter, a low-pass filtered PWM signal, produced by the MCU, is used as the control signal defining the output of the TEC driver. Optionally, a discrete Digital-to-Analog Converter could have been used, but this would have unnecessarily increased the complexity as well as the total cost of the system. The unity-gain Sallen–Key low-pass filter designed for the purpose of control signal filtering can be seen in figure 25. After filtering the PWM, the remaining DC-component with minimized ripple, acting as the control signal, is applied to the CONT pin of the ADN8833 (figure 20). The control signal voltage at the CONT pin has to be chosen from between 0 V and 2.5 V (due to the ADN8833 internal 2.5 V reference) according to the desired voltage over the controlled TEC element. Voltage of the filtered control signal can be varied by changing the duty cycle of the initial PWM control signal. When designing a DAC filter, a compromise has to be made between the maximum rate of change of the filtered DC voltage and the peak-to-peak magnitude of the residual ripple of the DC voltage. A higher cutoff frequency allows for faster rate of change, whereas a lower cutoff frequency reduces the ripple. As the process variable (temperature) has a rather slow rate of change, low ripple was preferred over speed.

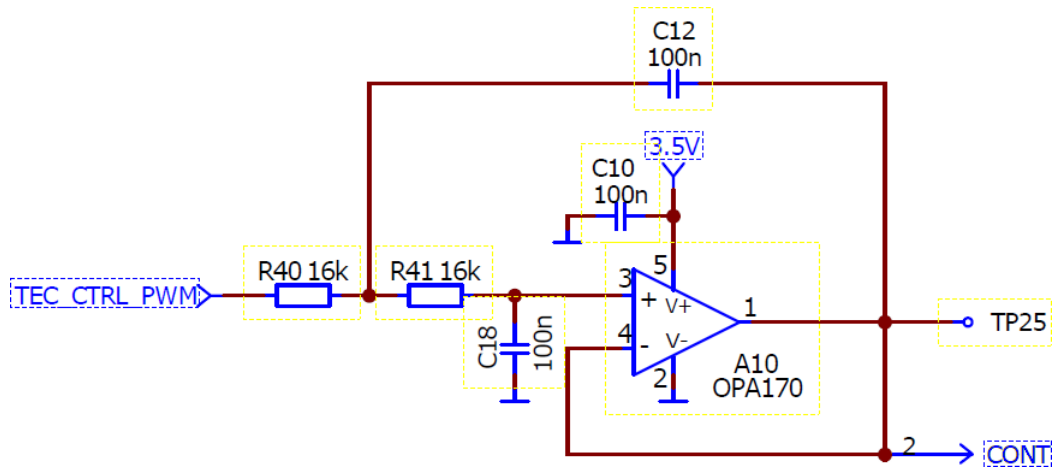


Figure 25. An enlargement of figure 20 showing the circuit diagram of the unity-gain Sallen–Key low-pass filter used to convert the MCU’s PWM output to a digital-to-analog converted output.

For the -3 dB corner frequency f_c of 1 kHz, the required resistance values (R40 & R41) were calculated using equation

$$f_c = \frac{1}{2 \cdot \pi \cdot \sqrt{R40 \cdot R41 \cdot C12 \cdot C18}}, \quad (15)$$

where both C12 and C18 were set to 100 nF, resulting to a required resistance of approximately 16 k Ω for both of the resistors R40 and R41 [95]. Capacitor C10 seen in figure 25 is used to filter high-frequency noise off the supply voltage of A10.

4.5.4 Heat dissipation

As thermoelectric coolers inevitably produce heat while being used for cooling, as described in (3.5), there is a need to dissipate the generated heat away from the component package and the PCB. For the TEC elements of the detectors used in the prototype, an estimated maximum heat dissipation of 0.5 W/cm² is required. Proper heat dissipation is crucial for reaching the desired temperature set point at the cold side of the TEC element [72, 93]. The detectors used are quite similar in terms of requirements for thermal design because both are enclosed in a TO-8 metal can package similar in size, and the TEC elements are placed so that their hot side is in contact with the bottom surface of the component package (see *IR Detectors Users Guide* [93] for detector type 1, and *Characteristics and use of infrared detectors* [72] for detector type 2). Thus, both of them

dissipate heat mainly through the bottom surface area of the component package. To ensure desired operation of the thermoelectric cooler, it is essential to create a path of least thermal resistance between the detector package's bottom surface area and the heat sink solution used (figure 26).



Figure 26. A photograph of the metallic tensioner plate attached to detector type 1. The plate is used both as a mechanical fastener and a thermal contact between the detector's bottom surface and the aluminum body of the optical cuvette.

Using only the component lead wires and/or the fastening bolt in the case of Detector type 1 (4.3.1), or only the component lead wires in the case of Detector type 2 (4.3.2) would *not* provide sufficient heat removal to allow nominal operation of the TEC [72,93]. The detector components are fastened to the base section of the optical cuvette using a milled screw-on aluminum tensioner plate. When tightened well leaving only a very small air gap, this piece of metal should offer an adequate passage for the heat to be conducted away from the detector package and further away into the main body of the optical cuvette (also made of anodized aluminum). Thermally conductive silicon paste could be spread between the detector's bottom and the tensioner plate to further reduce thermal resistance. Eventually the heat will dissipate out of the optical cuvette by means of natural convection, for the most part. The body of the optical cuvette has a slatted/perforated outer surface resembling that of a flared fin heat sink, which further improves heat dissipation by increasing the total surface area that can dissipate heat by natural convection.

The MCU is packed in a compact 48-pin Very Thin Quad Flat Non-Leaded package with a thermal pad at the package's bottom surface. In addition to the MCU itself, the setup includes a *Joint Test Action Group* industry standard debug port (connector X4) and a red LED indicator (V9), as well as an external 16 MHz crystal oscillator. Capacitors C16, C17, C47, C72, C73, C82, C83, and C90 (seen in figure 27) are used to filter electronic noise, if such would ever enter the system caused by, for example, any kind of an unexpected transient event. The pins left unused are connected to test points making their deployment possible in the event of an undesirable design error or other unexpected need. The pin configuration of the MCU, supplemented by additional notes regarding the operation of the MCU, can be reviewed in Appendix 1.

The built-in multi-channel 12-bit successive approximation register ADC of the MCU is used for the A/D conversion of the amplified measurement signal from the detector and all the other measurements necessary for operating and controlling the prototype. The ADC is fully configurable by embedded software. Using the MCU's peripheral ADC module reduces overall system cost as well as the surface area required for the PCB layout [96]. The input range of the ADC is set by the embedded software to between 0 V and 2.5 V using the MCU's internal reference. Sampling frequency and sample count of the ADC can be set by sending a command to the MCU, which allows the user to choose the measuring interval.

4.7 Supply & operating voltages

Two alternative inputs exist for providing the main supply voltage of 15 V required to operate the prototype. The inputs are implemented using a generic screw terminal connector that allows using a laboratory power supply unit, and a 4-pin M4 female connector to which a Vaisala USB cable (part no. 219690) can be attached to in order to power the prototype using USB connection. The electronics related to the serial bus communication are designed by Senior Electronics Engineer Niskanen A. of Vaisala. Powering most of the prototype using USB connection should be a convenient choice as a serial port connection is included and used in any case, as the MCU is commanded and measurement data is logged via the serial bus using a personal computer. For the majority of the prototype's subsystems the 500 mA current delivery capability of USB 2.0 is above sufficient. However, the current demand of the ADN8833 TEC controller is above the 500 mA current output capacity of USB 2.0 because of the set maximum TEC current limit of the detector TEC elements, described in section (4.5). Hence, the temperature control electronics had to be powered using an additional input option. An external labo-

ratory power supply unit was chosen to be used for the purpose. Having separate power supplies for the low-power signal conditioning electronics and the relatively high-power TEC driver should also help in reducing potential issues related to electronic noise caused by electromagnetic interference.

The 15 V main supply voltage applied to the prototype has to be regulated to several smaller voltage levels in order to make it suitable to be used as the operating voltage of the different functional electrical subsystems included. This applies to all subassemblies of the prototype, excluding the supply voltage of the TEC driver, which can be set by the user in the laboratory power supply unit that is connected to the supply voltage screw-terminal input of the TEC driver circuit. Where necessary, regulating the supply voltage is done using Texas Instruments LP2951ACMM-3.3/NOPB low-dropout voltage regulator units with a programmable output [97]. An exemplary circuit diagram of one of the voltage regulator setups used can be seen in figure 28.

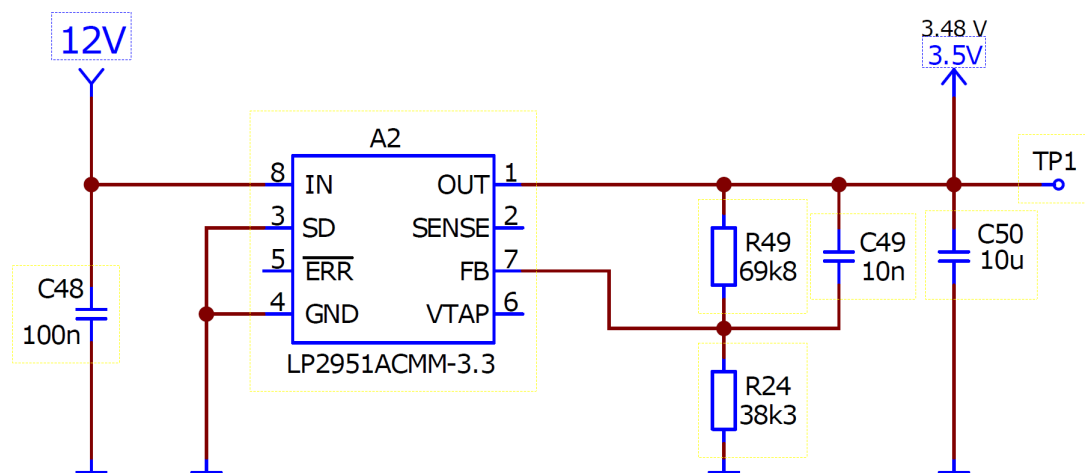


Figure 28. The voltage regulator circuit used to regulate the voltage from 12 V to 3.5 V. This same voltage regulator, manufactured by Texas Instruments, is used to accomplish all of the required operating voltages by modifying the voltage divider formed by resistors R49 and R24.

The required regulated voltage levels in order of magnitude are 3.3 V, 3.5 V, 8.0 V and 11.5 V. As 3.3 V is the nominal output voltage of the regulator used, output modification is not needed in the case of this regulated voltage level. Resistor values for the output voltage dividers used to obtain the other required voltage levels were calculated using

$$V_{\text{OUT}} = V_{\text{REF}} \cdot \left(1 + \frac{R_{\text{R49}}}{R_{\text{R24}}}\right) + I_{\text{FB}} \cdot R_{\text{R49}}, \quad (16)$$

where V_{REF} is the regulator's internal nominal reference voltage of 1.235 V and I_{FB} is the regulator's -20 nA nominal bias current for pin no. 7 (*FB*) [97]. For each of the regulators, the resistance value for the resistors corresponding resistor R24 was calculated by first choosing a general resistance value for the resistors corresponding R49. Functions executable using pins no. 2 (*SENSE*), 5 ($\overline{\text{ERR}}$) and 6 (*VTAP*) are not used and are thus left floating as recommended in the component's datasheet [97]. In addition to the regulated voltage levels, one voltage level higher than the 15 V main supply voltage level is required; the control electronics of the FPI filter (4.2) need a supply voltage of 34 V, which is implemented by using a customized multi-stage Dickson charge pump constructed using discrete components. The charge pump circuit is designed by Senior Electronics Engineer Niskanen A. of Vaisala.

5 PRINTED CIRCUIT BOARD DESIGN

Factory-made & automatedly assembled PCBs were used as the electronics development platform of the designed prototype. Using a solderless prototyping breadboard or even a solderable copper clad perfboard of any kind is out of question for noise-sensitive and complex (both mechanically and by the electronics used) systems like the one proposed in this thesis. All of the subsystems except the detector temperature control system had been already verified by earlier experiments, which further supported the use of PCBs as the development platform. The PCB layout was designed using PADS® Layout.

5.1 General requirements & design rules

As the designed device is a prototype intended solely for research and development use, not many strict requirements such as low manufacturing cost or a specific form factor (meaning the physical shape and size of the PCB) were posed for the PCB design. From a practical point of view regarding the limited time available for carrying out the thesis work, a fast delivery time was desirable but not considered as a necessary requirement. Design rules regarding object clearance and routing were set so that they meet with the production capability and design rule guidance of the PCB supplier and assembler chosen to manufacture the PCBs. The clearance rules set are shown in figure 29.

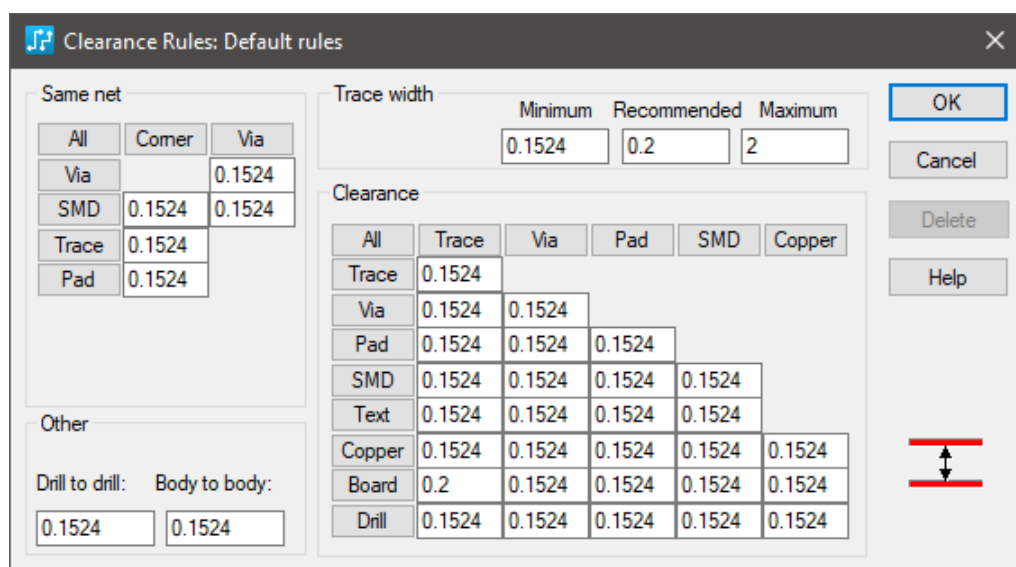


Figure 29. Default clearance and trace width rules set for the PCB design.

The optical cuvette used created the only few mechanical requirements for the PCBs. These included both the location and orientation of the IR source and detector components, as well as the location of the mounting holes used to attach the circuit board to the optical cuvette using screws. The source and detector components had to be mounted on the bottom side of the PCB, which would be the side facing towards the optical cuvette. The board outline is rectangular by shape and has rounded corners for comfortable handling. The top side projection of the PCB is 80 x 120 mm by size. It will be possible to greatly reduce the size of the PCB in possible future versions - this is because once the prototype has been found to function as desired, more components can be placed on the bottom side of the PCB.

5.2 Layer setup & interconnections

A total of four signal layers were deployed, since increasing the number of layers drastically simplifies the manual routing process and helps in minimizing current loop area. Having multiple layers with ground and power planes also provides better protection for electromagnetic interference due to the *image plane effect* [98]. Open plated-through hole vias with a drill diameter of 0.4 mm and a plate width of 0.2 mm were used for the interconnections between the layers of the PCB. The vias were intentionally left non-tented to promote testability, and to enable minor modifications to be made if such would be needed. Thermal vias were placed under the MCU (4.6) and TEC controller (4.5) for additional heat removal. Thicknesses of the different layers are listed in table 4.

Table 4. Build-up of the PCBs.

Name	Type	Thickness (μm)
Solder mask	Coating	N/D
Top	Component	35
Prepreg	Substrate	110
Layer 2	Plane	35
Prepreg	Substrate	1200
Layer 3	Plane	35
Prepreg	Substrate	110
Bottom	Component	35
Solder mask	Coating	N/D

All of the signal layers have a fully covering copper pour on them - the copper planes formed are used either as ground planes that are assigned to the analog ground (layers 1, 2 and 4) or power planes assigned to the 12 V net (layer 3). The 12 V net was chosen as the power plane voltage level as it is regulated to many smaller voltage levels at various locations around the PCB. A copper cutout restricting thermal conduction was placed near the μG IR source to all of the copper layers in order to reduce the possibility of heat conducting from the IR source to the photodetector. The copper cutout can be seen as the pale strip next to and below the 4-pin IR source component, in figure 30.

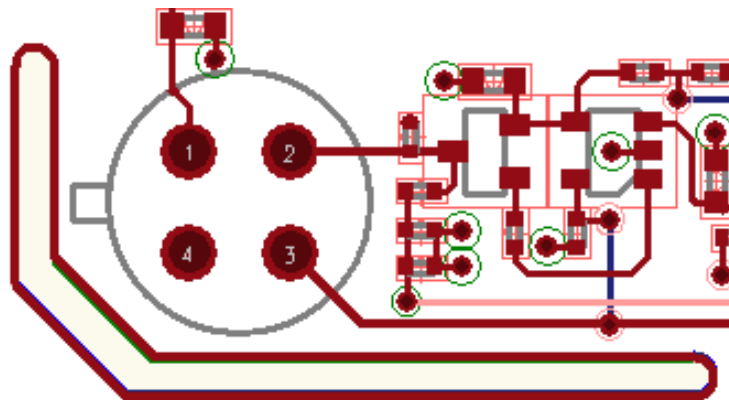


Figure 30. A screenshot of a section of the PCB layout, showing the thermal copper cutout surrounding the Vaisala μG IR emitter.

5.3 Component layout & routing

As described in the beginning of Chapter 4, two PCB variants were designed as two detectors enclosed in different kinds of packages were used to test the prototype. The layout of these two PCB variants is mostly identical, except for mounting the detectors. The component layout was designed starting from the largest components (connectors) followed by the accurate placement of the source and detector components. Then, the MCU was placed so that all the subsystems connecting to it could be placed as optimally as possible. After that, the most critical subsystems of the prototype were placed where possible considering the optimality of the signal path lengths, as well as the general good practices instructed in the datasheets and application notes of each of the components.

The layout is arranged so that the components likely to produce most electromagnetic interference are located as far away as possible from the most noise-sensitive parts. In

practice, this means that the TEC controller (4.5), the supply voltage inputs (4.7) and the serial bus interface are placed so that the copper traces related to them do not intersect with the photodetector measurement signal routes at any point. The signal produced by the photodetector was protected from noise sources by appropriate component placement and by keeping the copper trace through which it passes across as short as possible. Whenever possible, the same practice was applied to the copper traces associated with other measurement signals too. However, the signal produced by the photodetector was considered as top priority and the path it travels through was thus secured even though it caused the paths taken by some other measurement signal routes to not be at their most optimal. Majority of the components were placed on the top side of the circuit board to promote testability and modifiability, as can be seen in figure 31 showing the 3D model of the PCB. Test points were placed close to the operationally critical sections of the prototype for the same purpose. Only the pin receptacles used to mount the source and detector components to the PCB were placed on the bottom side.

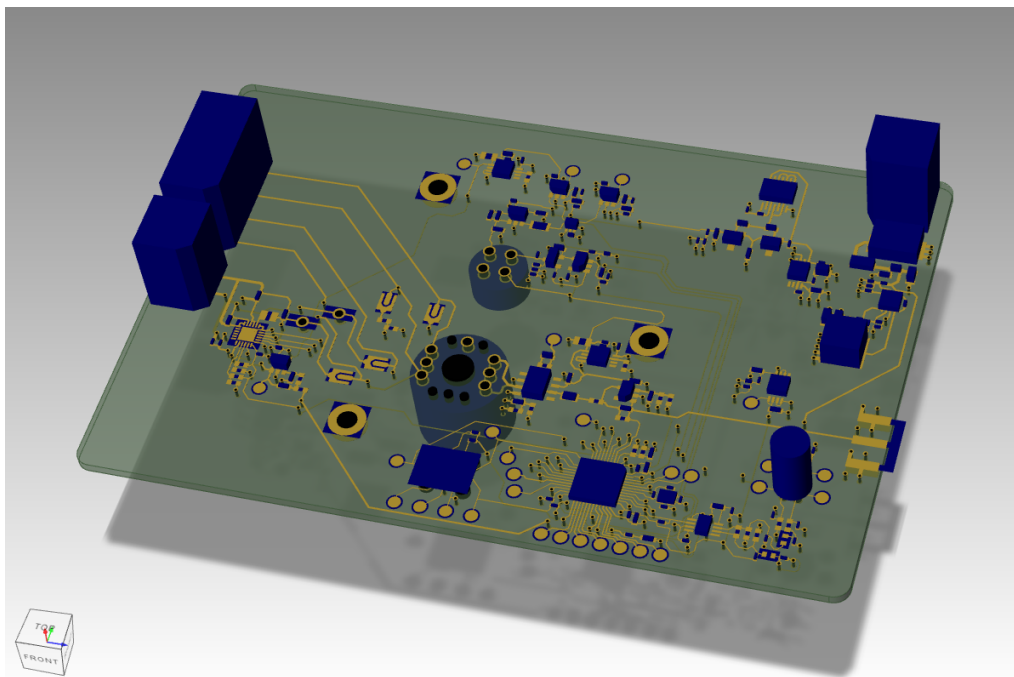


Figure 31. 3D model of the PCB (*detector type 1* variant). Vast majority of the components were placed on the top side of the PCB - only the IR source and detector components are located at the bottom side.

Four solderable jumpers, acting as near zero-ohm links, were included to allow the use of an external detector TEC controller by leaving the links open, if desired. Respectively

closing the links utilizes the temperature control circuit integrated onboard the PCB. The jumpers can be seen in figure 31 above the mounting hole closest to the bottom edge of the image. Solderable jumpers were chosen instead of zero-ohm resistors, because when operated with maximum voltage and current, the power consumed by the TEC can theoretically reach over 600 mW. If zero-ohm resistors would have been used, their package would have had to be quite large because of the theoretical maximum power they would have to withstand. In addition, solderable jumpers are easier to operate with; they can be closed by adding a sufficient amount of solder and opened using desoldering braid.

5.4 Automated error checking

The design was first inspected thoroughly by visually reviewing each of the subsystems and traces in order to detect any clearly visible design faults. Lastly, the automated design rule check feature of PADS®, called *Verify Design* (figure 32), was used to make definitively sure that no clearance or connectivity related design errors exist in the layout.

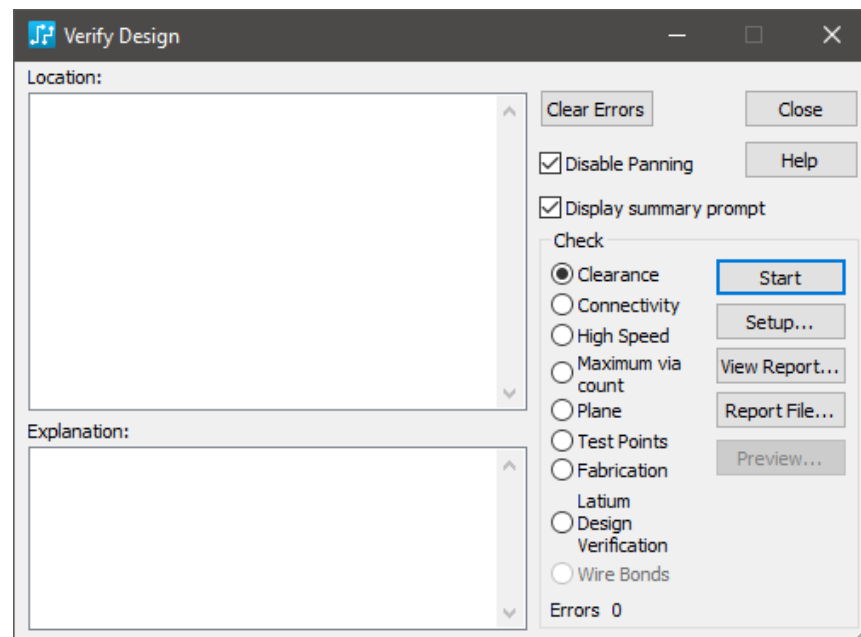


Figure 32. A screenshot showing the dialog box of the *Verify Design* feature of PADS® Layout.

Both of the automated error checks performed returned a clean ****NO ERRORS FOUND**** notification, meaning that the PCB layouts had been designed as intended in their electrical circuit diagrams.

6 EVALUATING OPERATION OF THE PROTOTYPE

In this chapter, the measurement setups used to test the functionality of the prototype, as well as the results obtained, are introduced. Successfulness of the electronics and PCB design is considered by comparing the measurement results to the design calculations and simulation-based estimations & expectations, where applicable. Finally, proposals for future work and further research are given.

6.1 Description of experiments

A total of five experiments were conducted for the prototype within the framework of this thesis in order to ensure desired operation of each of the designed subsystems included:

- **Experiment A – basic operation of the prototype:** First, to ensure that the PCBs do not contain significant manufacturing defects or major design faults, supply voltage was connected alternately to the two different inputs available, and the TEC driver supply voltage input separate from the other two inputs. Voltages of all the test points and regulator outputs were measured.
- **Experiment B – μG IR source control electronics:** it was first verified that a sufficient amount of power is supplied to the μG IR source by measuring the voltage over it. In addition, the power supplied to the IR source was manually changed, proving that the μG operating voltage control electronics work as intended.
- **Experiment C – FPI filter control electronics:** the FPI filter control electronics were tested by setting different output values for the related PWM control signals. By measuring, it was verified that the output voltages are of right amplitude, and that the switch used to change between the two voltages operates nominally.
- **Experiment D – photodetector signal amplification:** the amplified baseline signal level of both of the photodetector variants was measured to confirm that the amplifier setup works as it is supposed to.
- **Experiment E – TEC driver:** first, a small resistive load was used to simulate a TEC element in order to test that the voltage level and the amount of current flowing through the actual TEC would not exceed their set maximum limits. Then, the temperature of an actual detector TEC was controlled in order to ensure operation of the designed control circuit and the digital control loop.

6.2 Measurement setups

All of the experiments described in section 6.1 were performed using the same basic measurement setup, seen in figure 33. The PCBs were attached to an optical cuvette, which was then enclosed inside an aluminum measurement chamber. A small part of the optical cuvette can be seen as the black section between the PCB and the measurement chamber. In the measurements performed within the framework of this thesis, the chamber was used to reduce the possible effects of ambient IR radiation and variation in the background concentration of the target gas in the laboratory premises. The two vertically aligned tube fitting mounting holes, seen at the side of the chamber, were blocked for the duration of the experiments.



Figure 33. A photograph showing the PCB attached to an optical cuvette enclosed inside a sealable measurement chamber. The chamber can be used to perform measurements with known gas concentrations, by attaching tube fittings to the two threaded holes visible on the side of the chamber.

During each experiment, the PCB was powered using a Vaisala 219690 USB cable. The cable was connected to a laptop computer at one end, and to the threaded vertical 4-pin M8 male connector of the prototype (seen near the lower right corner of the PCB in figure 33) at the other end. Experiment E required the use of an additional laboratory power supply unit because of the current demand of the TEC element, described in more detail in section 4.7. The bench power supply unit used is a Keysight Technologies E36103A, a programmable DC power supply with a maximum output rating of 20 V, 2 A and 40 W.

Measurement data related to **Experiments A, B, C & D** was captured using a Tektronix DPO3014 oscilloscope. The ground lead of the oscilloscope probe used was connected to the PCB's analog ground, which acts as the reference point for the electronics. Voltages and waveforms of the different subsystems tested were then inspected one by one to meet the objectives of Experiments A–D. Measurement data obtained from **Experiment E** was acquired using a Fluke 179 True RMS Multimeter, and by logging thermistor temperature data on a personal computer via serial bus by operating the prototype using a command-line interface. The experiment was conducted by first simulating the integrated TECs of the detectors, using a set of power resistors. Three power resistors, with a nominal resistance of 1.3Ω and maximum power dissipation of 25 W each, were connected in parallel to achieve a total resistance resembling that of a miniaturized Peltier element and having a sufficient power dissipation capability. The resistor pack was connected to the output of the TEC driver. For the duration of this experiment, the actual TEC element (inside the detector package) was separated from the TEC driver output by leaving the solderable jumpers - included on the PCB for this purpose - in the *open* position. After desired action of the TEC driver had been confirmed, the solderable jumpers were closed and the integrated TEC element of a photodetector was tested.

6.3 Results & discussion

Experiment A produced the results shown in table 5. All of the regulated and boosted voltage levels were within an acceptable error range, and nothing of unexpected nature was observed when voltages of the test points of the PCB were inspected one by one. The voltage levels shown in the **Nominal [V]** column of table 5 are the target values of the different voltages needed for operating the prototype. The values shown in the **Measured [V]** column are averages of the measured voltage levels of three measurement iterations. After ensuring that the operating voltages of the PCB were nominal and before performing Experiments B–E, the embedded software developed for the prototype was flashed to the MCU using the RS-232 serial bus, allowing full control of the prototype's features.

Table 5. Measurement data from Experiment A: voltages of the test points and regulator outputs.

Nominal [V]	Measured [V]
34.00	34.40
15.00	15.20
12.00	12.80
11.50	11.80
8.00	8.18
3.50	3.43
3.30	3.37

Then, after flashing the firmware into the MCU, the prototype started successfully when supply voltage was applied to it, regardless of the supply voltage input used. The results of Experiment A indicate that the electronics associated with the operating-power related functionalities of the prototype (see section 4.7) were successfully designed. This includes the different supply and operating voltages of the prototype, as well as the serial bus used for flashing and commanding the MCU. The ripple and noise characteristics of the operating voltages could be further investigated using an oscilloscope or a spectrum analyzer, as such properties could potentially adversely affect the operation of the prototype.

The observations and results from **Experiment B** can be interpreted from figure 34.

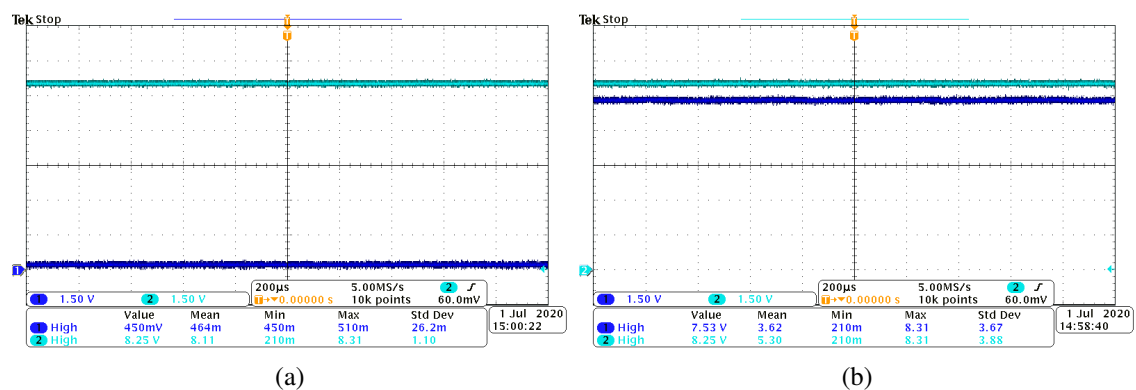


Figure 34. Voltages measured as part of Experiment B. Two μG IR source operating voltages, a higher (34a) and a lower (34b), were tested. The operating voltage of the IR source can be calculated by subtracting the control voltage level (blue) from the constant supply voltage (turquoise).

Subfigures 34a & 34b show the measured potential difference over the μG IR emitter, using two different control signal voltages. In both of the subfigures, the turquoise voltage signal is the IR source's constant supply voltage of 8.25 V, and the blue voltage signal is the software-selectable control signal voltage that defines the actual operating voltage of the IR emitter as the potential difference between the constant supply voltage and the control signal voltage. Subfigure 34a shows a larger operating voltage of 7.8 V applied over the emitter, whereas subfigure 34b shows a smaller operating voltage of 0.72 V. As the constant supply voltage of 8.25 V remained stable and the control signal voltage could be set as desired, Experiment B essentially proved that the control electronics for the IR source (see section 4.2) work as intended. The control electronics allow the user of the prototype to either manually set different operating voltages for the IR source, or to modulate the operating voltage of the IR source using a software-based control loop. In practice, the IR source can be modulated by switching the control voltage between a higher and a lower voltage at a desired frequency using a digital control loop.

Experiment C produced the measurement results shown in figure 35.

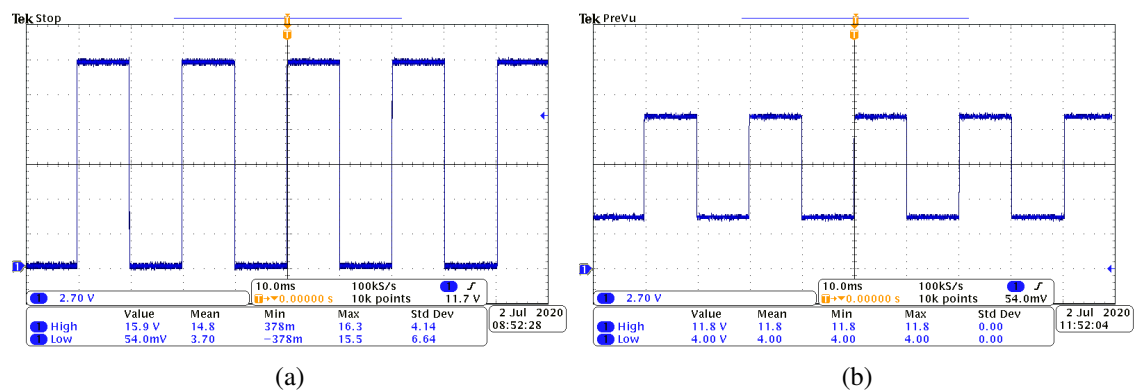


Figure 35. Two oscilloscope screen captures obtained as part of Experiment C, showing that both the *High* and *Low* operating voltages of the FPI filter can be manually set.

The FPI filter's operating voltage was measured using a single oscilloscope probe placed at the positive input terminal lead of the FPI filter. The ON voltage was initially set to 15.9 V and the OFF voltage close to 0 V, seen as the measured *High* and *Low* voltage levels in figure 35a. The ON and OFF voltages were then changed, one after the other, so that the ON voltage was reduced and OFF voltage was increased. Figure 35b shows the operating voltage waveform after both of the changes had been made. It was thus shown that the voltages can be individually set to desired values, corresponding to the pass-band wavelengths of interest, within the supply voltage range of the FPI filter. Essentially,

Experiment C demonstrated that it is possible to set two different supply voltages, independent of each other, for the FPI filter incorporated in the prototype's optical path.

Before performing **Experiment D**, a small modification had to be made to all of the PCBs. The reason was, that on preliminary tests it was found out that the waveform of the amplified photodetector measurement signal was not quite as it was expected to be. The amplification circuit worked in principle, as the signal was indeed amplified to a measurable voltage level, but the signal was not square-wave shaped as it should have been, as can be seen in figure 36. Various alternative possible causes were examined, including the possibility of amplifier bias voltage swing, and the possibility of too weak a 1st stage amplifier gain. However, these options could not explain the problem. Finally, detailed AC-analysis simulation of the amplifier setup revealed the most plausible explanation.

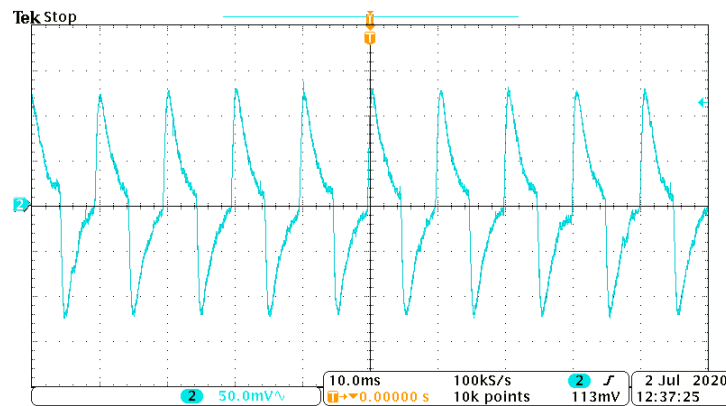


Figure 36. An oscilloscope screen capture showing the overshoot problem related to the photodetector measurement signal amplification setup, detected prior to performing Experiment D.

The apparent cause for this undesired behavior was the phase shift created by the combination of the DC-decoupling capacitor C11 and the 2nd stage amplifier's input resistor R38 (see figure 18 for reference), which caused the system to be unstable over the measurement frequency range. The problem was fixed by choosing a higher resistance value for the 2nd stage amplifier's input resistor R38, effectively decreasing the reactive part of the series impedance and significantly reducing the phase shift of the series impedance from about -35° to approximately -0.34° at the frequency of 100 Hz. Alternatively, capacitor C11 could have been replaced, but a capacitor of sufficiently high capacitance in a suitably sized component package was not available at short notice. After modifying the PCBs, Experiment D could be carried out. The amplified signal of both of the photodetectors (presented in sections 4.3.1 & 4.3.2) expectedly appeared as a square wave waveform,

as shown in figures 37 and 38. The amplified photodetector measurement signals were obtained operating at two different modulation frequencies. Both of the measurements were performed using the oscilloscope in AC coupling mode to remove the 1.25 V DC offset off the signal, as well as to maximize the oscilloscope's resolution.

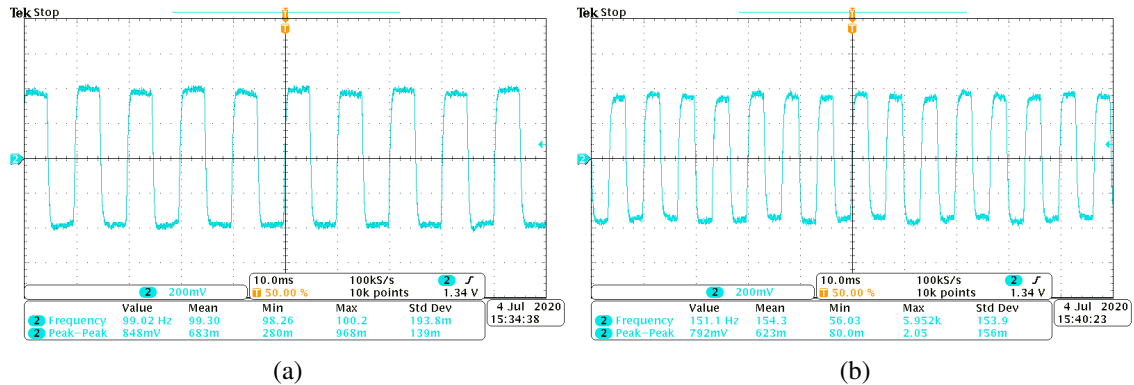


Figure 37. The amplified measurement signal of the Hamamatsu photodetector (4.3.2) with modulation frequencies of 100 (a) & 150 (b) Hz.

As can be seen by comparing figures 37a & 37b, the modulation frequency was successfully changed by commanding the MCU. Based on the measurements, the amplified peak-to-peak voltage of the Hamamatsu detector appears to vary around 800 mV depending on the background concentration of the target gas. Some noise can be seen in the amplified response of the photodetector, though it is not possible to determine the exact quantity or source of it on the basis of the measurements made. The possible noise sources, such as variation of the target gas concentration within the prototype's optical path, are uncertain by their significance. Figure 38 shows the amplified signal of the VIGO detector.

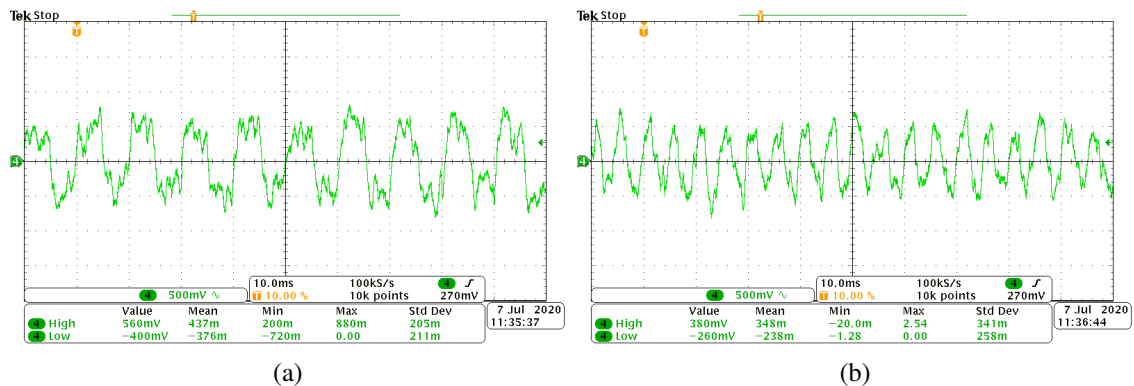


Figure 38. The amplified measurement signal of the VIGO photodetector (4.3.1) with modulation frequencies of 100 (a) & 150 (b) Hz.

Again, the modulation frequencies of 100 & 150 Hz were used, as seen in figures 38a & 38b. The peak-to-peak voltage of the VIGO detector was about the same as that of the Hamamatsu detector's, being approximately 800 mV by average. However, the SNR of the amplified signal produced by the VIGO photodetector seemed to be much smaller. This should be mostly due to the larger difference in size between the active area of the VIGO detector and the emitter area of the IR source used – the detector's active area is only about 1% of the size of the IR source's emitter area. This grand difference in size leads to only a very small portion of the IR radiation to be collected by the photodetector, making noise a dominant part of the measurement signal. Experiment D showed that not all the necessary aspects were initially taken into account when designing the amplifier setup for the photodetector measurement signal. After finding out the likely root cause of the stability-related issue and modifying the component values, the amplifier setup could be, however, fixed to work as originally intended. The difference between the responses of the two different photodetectors tested was significant. This difference in performance would presumably narrow substantially, if the active areas of the detectors would be equal in size. The measured peak-to-peak voltage of both of the photodetectors tested still leaves some margin for raising the gain of either the 1st or the 2nd amplifier stage, as the input range of the ADC is 0.0–2.5 V and the photodetector signal has an offset of +1.25 V.

First part of **Experiment E** was performed using a set of power resistors and a multi-meter, as described in section 6.2. By commanding the MCU, the control signal voltage fed to the ADN8833 TEC controller was manually set to first correspond to the maximum possible voltage across the TEC element, and then to the minimum voltage over the TEC (being desirably as close to 0 V as possible). The voltage over the power resistor pack and the current flowing through it were then measured. The maximum voltage was measured to be 0.887 V and the maximum current, respectively, 635 mA. This would suggest that the voltage and current limits set for the quantities in section 4.5.1 work as designed. In addition to the maximum values, applying the OFF-state control signal voltage was tested. When the control signal voltage was set to the OFF state, the voltage measured over the power resistor pack was 0.001 V and the current flowing through it 0.001 A, respectively. The polarity of the voltage was correct within the control signal voltage range corresponding to the experimentally observed TEC voltage range limits of 0 to 0.887 V, meaning that also the direction of the current flow would be correct and the TEC element would operate in cooling mode. After the limits of magnitude of the TEC voltage and current, as well as the polarity of the voltage and the direction of current flow had been experimentally found to be proper, the second part of Experiment E was carried out.

The second part of Experiment E (figures 39 & 40) was done using the digital proportional–

integral temperature control loop implemented in the embedded software. The temperature of the Hamamatsu detector's integrated TEC element was adjusted to three different temperature set points: +20, 0 and -30 °C. The experiment was conducted in the room temperature of about +27 °C, meaning that the theoretical ΔT_{MAX} of the TEC element (see section 4.3.2) could not have precluded the experiment. With the proportional and integral terms chosen, the system's response showed no noticeable oscillation during settling. Correspondingly, the settling time of the system was quite slow depending on the set point temperature chosen. The higher the ΔT , the longer the system's settling time. The settling times for the different temperature set points were approximately 2 minutes for 20 °C, 3 minutes for 0 °C and 6 minutes for -30 °C. Once the temperature set point had been reached, the temperature remained close to the set point value. After stabilizing to the set point, the temperature varied within an error range of $\leq \pm 0.05$ °C. This level of accuracy should be sufficient in the application.

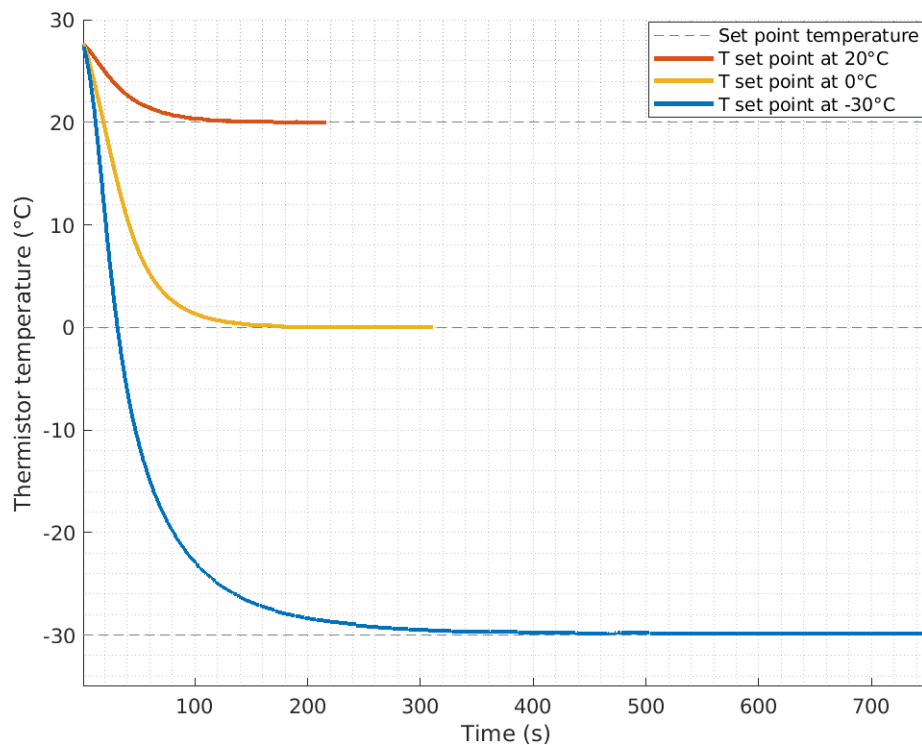


Figure 39. The Hamamatsu photodetector's integrated TEC was cooled down to three temperature set points (+20, 0 & -30 °C) to ensure desired operation of the TEC driver.

In addition to acquiring the temperature data, the photodetector measurement signal was measured once the temperature set points had been reached, in order to find out how

operating the TEC controller affects the signal. The effect of operating the TEC controller can be seen in figure 40. On preliminary assessment, it quite clearly appeared that the amount of noise in the photodetector measurement signal increased when the TEC controller was used to control the temperature of the photodetector. The phenomenon can be most clearly noticed by comparing the measured waveforms of figures 37a & 40.

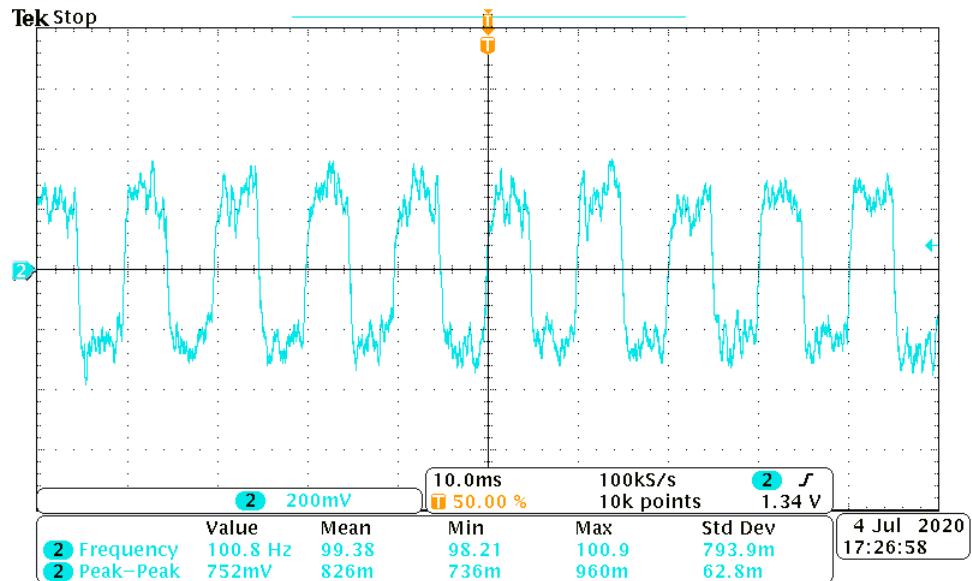


Figure 40. An oscilloscope screen capture showing an increase in the amount of noise present in the amplified photodetector measurement signal, when the TEC controller was being used for cooling the photodetector.

The main findings of Experiment E can be summarized as follows. The TEC driver and the associated electronics work as designed, making it possible to set and control the temperature of the integrated TEC element of the photodetectors tested. However, as using the TEC driver seems to produce a considerable amount of noise to the photodetector's signal, the desired benefit of cooling the detector was not achieved. The cause of this adverse effect needs to be identified among the other topics of further research.

6.4 Future work

From a purely performance-centric point of view, it can be stated with great certainty that the design could be further optimized by making component choices based not on

established practices and availability, but instead on the factors that most significantly affect the operation of the prototype. For the most part the component choices were made reasonably, but in some respects this situation was not fully achieved due to problems in component availability. From the point of view of possible future productization of the concept, the matter is slightly different, however. Considering productization, the design should be further unified, which in this context would mean reducing the number of different components used to a minimum, as well as choosing less expensive components of sufficient quality. In addition, it would likely be a good idea to evaluate the possibility of using only typical passive component values that are generally available (meaning component values included in some of the commonly used E series of preferred numbers) to reduce the possibility of production-related availability problems – however this should preferably not be done at the expense of performance.

The photodetector measurement signal amplifier setup design should be once more evaluated in detail and optimized, and then, if it turns out to be necessary, the use of other possible amplification implementations could be considered. In addition to the amplifier setup, the TEC control circuit requires further evaluation. The proportional and integral terms of the digital control loop could be further optimized using the heuristic Ziegler–Nichols method, or similar. Then, the performance of the TEC controller (4.5) should be benchmarked in chosen temperature set points using the Thorlabs TED200C (briefly mentioned in section 1.2 and seen within the block diagram in figure 13) as a reference. The exact cause of the noise observed in the photodetector measurement signal, related to the TEC control circuit, should be investigated and thoroughly understood so that the amount of noise caused by the temperature control electronics can be reduced by implementing appropriate design changes. If it is decided that the use of the TEC controller is continued after optimizing the associated circuit, tests in different temperatures, humidities and other controlled environmental conditions should be performed to see whether the TEC controller performance is sufficient in changing environments and the gas sensor performance remains good. On the other hand, if no clear solution to the noise problem is found, the use of other PCB-attached alternatives for implementing the temperature control functionality could be considered. After these steps of further research have been executed, the prototype’s performance should be defined by measuring known concentrations of the target gas and defining the signal-to-noise ratio of the measurement signal produced by the photodetector. This should eventually make it possible to estimate the accuracy, precision and resolution of the sensor. Taking these steps of future work should allow defining the need for changes in the electronics and PCB design in order to reach the desired level of performance.

7 CONCLUSION

The aim of this master's thesis was to combine previously created separate prototype designs and functionalities proven to work, related to the development of a novel optical gas sensor. For this purpose, a single-circuit-board prototype, that could be easily used for testing the performance of the concept, was designed and implemented. As a novel feature, electronics required to control the temperature of a TEC integrated inside a photodetector were designed. For future reference, it should be noted that considerable care is required when designing multi-stage amplifier setups. In particular, impedance loads with a significantly high reactive component do affect the operation of operational amplifiers - a phenomenon that could have been detected earlier on than it was by accurate and more versatile simulation and by having a closer look at the related theory. Perhaps the single most significant highlight related to the design work done is the TEC controller integrated on the PCB. Designing and testing this kind of an integrated solution for controlling the detector's temperature has significant novelty value within the framework of the ongoing research & development work related to the topic of this thesis.

In addition to the design work done, early stage tests were performed as part of of this thesis in order to confirm basic operation of each of the subsystems incorporated in the prototype. The experiments performed were delimited to ensuring that the prototype works as designed and desired. Based on the experiments performed for the prototype, the objectives set for the work were all achieved. The IR emitter as well as the voltage-tunable FPI filter could be controlled appropriately and the measurement signal produced by the photodetector was successfully amplified to an adequate voltage range. Tests performed with the integrated TEC controller provided promising results, however optimizing and evaluating performance of the design should be continued. Most of the functionalities worked as intended right away, however some of them required minor changes to be made, mainly limited to modifying individual component values. It should be noted that such need of modifying the design is an expected, inherent and normal part of any kind of prototyping. The main results of this master's thesis are the prototype electronics and PCB designed. The electronics and PCB designed are an essential part of an optical gas sensor prototype that allows easily testing a rapid-measurement concept by measuring known concentrations of the target gas. Altogether, the implemented prototype managed to meet the fundamental criteria and requirements set for its operation. Once the follow-up actions proposed in section 6.4 have been made, the prototype and the information obtained by testing and using it should allow evaluating the concept's feasibility more comprehensively than was previously possible.

REFERENCES

- [1] British Broadcasting Corporation. *The Canary In The Coal Mine Isn't Ancient History*. [Web article], 2016 (originally published in 1986). [Online; accessed May, 8, 2020]. Available at: http://news.bbc.co.uk/onthisday/hi/dates/stories/december/30/newsid_2547000/2547587.stm.
- [2] Denver Post photographer. *Rabbit Used To Test For Nerve Gas At RMA*. [Photograph], 1970. [Online; accessed May, 4, 2020]. Retrieved from: <https://www.loc.gov/pictures/item/co0168.photos.316333p/>.
- [3] Peterson M. & Talcott P. *Small Animal Toxicology*. Saunders, an imprint of Elsevier Inc., 3rd edition, 2013.
- [4] Kumar A. et al. *Application of Gas Monitoring Sensors in Underground Coal Mines and Hazardous Areas. International Journal of Computer Technology and Electronics Engineering (IJCTEE)*, 3(3):9–23, 2013.
- [5] Bogue R. *Detecting gases with light: a review of optical gas sensor technologies. Sensor Review*, 35(2):133–140, 2015.
- [6] Bogue R. *Technology Roadmap: Optoelectronic Gas Sensors in the Petrochemicals, Gas and Water Industries*. [PDF file], 2006. [Online; accessed May, 7, 2020]. Available at: <http://userweb.eng.gla.ac.uk/charles.ironside/QCSENSEPrivate/GasSensinRoadmap.pdf>.
- [7] Vaisala Oyj. *Vaisala in brief*. [Web page], 2020. [Online; accessed May, 18, 2020]. Available at: <https://www.vaisala.com/en/about-vaisala/vaisala-brief>.
- [8] Vaisala Oyj. *About Vaisala*. [Web page], 2020. [Online; accessed May, 18, 2020]. Available at: <https://www.vaisala.com/en/about-vaisala>.
- [9] Mizoguchi Y. & Ohtani Y. *Response Characteristics of VAISALA CO₂ Sensors and its Correction for the accurate estimation of soil CO₂ efflux. AsiaFlux Newsletter*, 19:4–8, 2006.
- [10] Hevner A. et al. *Design Science in Information Systems Research. Management Information Systems Quarterly*, 28(1):75–105, 2004.
- [11] Xiao L. et al. *A Survey on Gas Sensing Technology. Sensors*, 12(7):9635–9665, 2012.

- [12] Mehta A. *Introduction to the Electromagnetic Spectrum and Spectroscopy*. [Web article], 2011. [Online; accessed May, 19, 2020]. Available at: <https://pharmaxchange.info/2011/08/introduction-to-the-electromagnetic-spectrum-and-spectroscopy/>.
- [13] Kumar P. & Mina U. *Fundamentals and Techniques of Biophysics and Molecular Biology*. Pathfinder Publication, New Delhi, India, 2nd edition, 2016.
- [14] The Editors of Encyclopædia Britannica. *Wave-particle duality*. [Web article] published by Encyclopædia Britannica, inc., 2016. [Online; accessed May, 24, 2020]. Available at: <https://www.britannica.com/science/wave-particle-duality>.
- [15] Ronan P. *EM spectrum*. [Picture], 2007. [Online; accessed May, 11, 2020]. Retrieved and adapted from: https://commons.wikimedia.org/wiki/File:EM_spectrum.svg under the CC BY-SA 3.0 license.
- [16] Baggott J. *Beyond Measure: Modern Physics, Philosophy and the Meaning of Quantum Theory*. Oxford University Press, 2nd edition, 2003.
- [17] Byrnes J. *Unexploded Ordnance Detection and Mitigation*. Springer Science+Business Media B.V., 1st edition, 2008.
- [18] Prange A. & Modrow H. *X-ray absorption spectroscopy and its application in biological, agricultural and environmental research. Reviews in Environmental Science and Bio/Technology*, 1:259–276, 2002.
- [19] Savin S. et al. *The applications of X-ray absorption spectroscopy in the study of nanocrystalline materials and electrochemical systems. Comptes Rendus Chimie*, 11(9):948–963, 2008.
- [20] Shouyuan T. et al. Applications and techniques of microwave spectroscopy. *Progress in Chemistry*, 21:1060–1069, 2009.
- [21] Wlodarczak G. *Microwave and Radiowave Spectroscopy, Applications*. In *Encyclopedia of Spectroscopy and Spectrometry*. Academic Press, an imprint of Elsevier Inc., 2017.
- [22] Dinh T.-V. et al. *A review on non-dispersive infrared gas sensors: Improvement of sensor detection limit and interference correction. Sensors and Actuators B: Chemical*, 231:529–538, 2016.
- [23] Popa D. & Udrea F. *Towards Integrated Mid-Infrared Gas Sensors. Sensors*, 19(9):2076, 2019.

- [24] Coates J. *Interpretation of Infrared Spectra, A Practical Approach*. In *Encyclopedia of Analytical Chemistry* (eds R.A. Meyers and M.L. McKelvy). John Wiley & Sons Ltd., 2006.
- [25] Asahi H. & Horikoshi Y. *Molecular Beam Epitaxy: Materials and Applications for Electronics and Optoelectronics*. John Wiley & Sons Ltd., 2019.
- [26] MIRO Analytical AG. *High-precision Multicomponent Gas Analyzer*. [Web page]. [Online; accessed June, 15, 2020]. Available at: <https://www.miro-analytical.com/Product.html>.
- [27] Thermo Nicolet Corp. *TN-00128 – FT-IR vs. Dispersive Infrared*. [Application Note], 2002. [Online; accessed June, 01, 2020]. Available at: http://www.thermo.com.cn/Resources/200802/productPDF_21615.pdf.
- [28] Vaisala Oyj. *Carbocap Sensor Illustration*. [Picture], 2018. [Material Bank of Vaisala Oyj; accessed May, 11, 2020].
- [29] Anderson R. & Wong J. *Non-Dispersive Infrared Gas Measurement*. International Frequency Sensor Association (IFSA) Publishing, S.L., 1st edition, 2012.
- [30] Walters C. et al. *The Spectrophotometric Analysis and Modeling of Sunscreens*. *Journal of Chemical Education*, 74(1):99, 1997.
- [31] Haigh M. et al. *Mid-infrared $Al_xIn_{1-x}Sb$ light-emitting diodes*. *Applied Physics Letters*, 90(23):231116, 2007.
- [32] Fanchenko S. et al. *LED-based NDIR natural gas analyzer*. *IOP Conference Series: Materials Science and Engineering*, 108:012036, 2016.
- [33] Asahi Kasei Microdevices Corp. *AKM releases three products suitable for NDIR flammable gas sensing: IR LED AK9703, IR sensor AK9730, and IR sensor AFE IC AK9723*. [Web article], 2020. [Online; accessed May, 25, 2020]. Available at: <https://www.akm.com/eu/en/about-us/news/2020/20200213-ak9703ak9730ak9723/>.
- [34] IBSG Co. Ltd. *LIGHT-EMITTING DIODE LED-430 - NS*. [Datasheet], 2013. [Online; accessed May, 25, 2020]. Available at: <http://www.ibsg-st-petersburg.com/datasheet/LED/LED-430-NS.pdf>.
- [35] Scholz L. et al. *MID-IR LED-based, photoacoustic CO_2 sensor*. In *Procedia Engineering Vol. 120, EUROSENSORS 2015*, pages 1233–1236. Elsevier Ltd., 2015.

- [36] Johnston S. *Gas monitors employing infrared LEDs*. *Measurement Science and Technology*, 3(2):191–195, 1992.
- [37] Fanchenko S. et al. *Multi-wavelength IR method for monitoring air pollution in cities*. In *2016 IEEE International Smart Cities Conference (ISC2)*, pages 1–6, 2016.
- [38] Rumyantsev S. et al. *Low frequency noise and long-term stability of noncoherent light sources*. *Journal of Applied Physics*, 96(2):966–969, 2004.
- [39] Hodgkinson J. et al. *Non-dispersive infra-red (NDIR) measurement of carbon dioxide at 4.2 μ m in a compact and optically efficient sensor*. *Sensors and Actuators B: Chemical*, 186:580–588, 2013.
- [40] Sato K. et al. *Comparative effectiveness of light emitting diodes (LEDs) and Lasers in near infrared photoimmunotherapy*. *Oncotarget*, 7(12):14324–14335, 2016.
- [41] Fujitsuka N. et al. *Alcohol Detection in Exhaled Air by NDIR Method*. *IEEJ Transactions on Sensors and Micromachines*, 132(7):219–223, 2012.
- [42] Mueller G. *Electroluminescence I*, volume 64 of *Semiconductors and Semimetals*. Academic Press, an imprint of Elsevier Inc., 1999.
- [43] Uotila J. *Comparison of infrared sources for a differential photoacoustic gas detection system*. *Infrared Physics & Technology*, 51:122–130, 2007.
- [44] Hodges M. & Schiessl U. *Lead salt tunable diode lasers: key devices for high-sensitivity gas analysis*. In *Proc. SPIE 3628, In-Plane Semiconductor Lasers III*, 1999.
- [45] Razeghi M. et al. *Quantum cascade lasers: from tool to product*. *Optics Express*, 23(7):8462–8475, 2015.
- [46] Normand E. & Howieson I. *Quantum-cascade lasers enable gas-sensing technology*. *Laser Focus World*, 43(4):90–92, 2007.
- [47] Electro Optical Components Inc. *Laser Gas Detection Using Tunable Diode Laser Spectrometry (TDLS)*. [Product catalogue], 2020. [Online; accessed May, 29, 2020]. Available at: <https://www.eoc-inc.com/lasers-ndir-gas-detection/>.
- [48] Sch; a user of Wikipedia. *Black-body spectrum for temperatures between 300 K and 10,000 K in a log-log diagram*. [Picture], 2006. [Online; accessed June, 1, 2020.]. Retrieved from: https://commons.wikimedia.org/wiki/File:BlackbodySpectrum_loglog_150dpi_en.png under the CC BY-SA 3.0 license.

- [49] Oshino Lamps Ltd. *What is NDIR?* [Web page]. [Online; accessed June, 03, 2020]. Available at: <https://www.oshinolamps.co.jp/en/ndir/nondispersive-infrared/>.
- [50] CMOS IR GmbH. *Homepage of CMOS IR GmbH.* [Web page]. [Online; accessed June, 02, 2020]. Available at: <https://www.cmosir.com/>.
- [51] Micro-Hybrid Electronic GmbH. *Homepage of Micro-Hybrid Electronic GmbH.* [Web page]. [Online; accessed June, 02, 2020]. Available at: <https://www.microhybrid.com/en/>.
- [52] Hawkeye Technologies Inc. *Homepage of Hawkeye Technologies, Inc.* [Web page]. [Online; accessed June, 02, 2020]. Available at: <http://www.hawkeyetechnologies.com/>.
- [53] Axetris AG. *Homepage of Axetris AG, a company of the Leister Group.* [Web page]. [Online; accessed June, 02, 2020]. Available at: <https://www.axetris.com/en>.
- [54] Alluxa Inc. *Alluxa Learning Center – What are thin-film optical filters?* [Web page]. [Online; accessed June, 04, 2020]. Available at: <https://www.alluxa.com/learning-center/what-are-thin-film-optical-filters/>.
- [55] Honsberg C. & Bowden S. *Anti-Reflection Coatings.* [Web page]. [Online; accessed June, 03, 2020]. Available at: <https://www.pveducation.org/pvcdrom/design-of-silicon-cells/anti-reflection-coatings>.
- [56] Paschotta R. (RP Photonics Consulting GmbH). *RP Photonics Encyclopedia.* [Web page]. [Online; accessed June, 02, 2020]. Available at: <https://www.rp-photonics.com/encyclopedia.html>.
- [57] Vaisala Oyj. *B211311EN-A – Infrared Sensor Technology and its Impact on HVAC CO₂ Measurement Accuracy.* [Application Note], 2013. [Online; accessed June, 03, 2020]. Available at: <https://www.vaisala.com/sites/default/files/documents/CEN-TIA-HVAC-CO2-Measurement-Accuracy-B211311EN-A.pdf>.
- [58] Rogalski A. *Infrared Detectors.* LLC, CRC Press, 2nd edition, 2010.
- [59] Ready J. *Optical Detectors and Human Vision*, volume TT79 of *Fundamentals of Photonics* edited by Roychoudhuri, C. The International Society for Optics and Photonics (SPIE), 2008.

- [60] Bass M. et al. *Handbook of Optics*, volume 1. Inc., McGraw-Hill, 2nd edition, 1995.
- [61] Stiens J. et. al. *Infrared Thermo-Electric Photodetectors*. In F. Duarte, editor, *Laser Pulse Phenomena and Applications*, chapter 8. IntechOpen, 2010.
- [62] Piotrowski J. & Rogalski A. *Uncooled long wavelength infrared photon detectors*. *Infrared Physics & Technology*, 46:115–131, 2004.
- [63] Zamboni J. *Integrated thermoelectric cooler/package for infrared detector array temperature stabilization*. In *Proceedings Vol. 5209, Materials for Infrared Detectors III*, page 173. The International Society for Optics and Photonics (SPIE), 2003.
- [64] Zoran J. *Micro and Nanophotonics for Semiconductor Infrared Detectors*. Springer International Publishing, 1st edition, 2014.
- [65] Huuhtanen M. *Optimal Mid-Infrared Photon Detectors for Use with Voltage-Tunable Filters in Gas Sensing Applications*. Master's thesis, Aalto University, School of Electrical Engineering, Finland, 2018.
- [66] Zumbahlen H., editor. *Linear Circuit Design Handbook*. Newnes, an imprint of Elsevier Inc., 1st edition, 2008.
- [67] Razavi B. *The Transimpedance Amplifier [A Circuit for All Seasons]*. *IEEE Solid-State Circuits Magazine*, 11(1):10–97, 2019.
- [68] Lee P. of Analog Devices Inc. *AN-940 – Low Noise Amplifier Selection Guide for Optimal Noise Performance*. [Application Note], 2013. [Online; accessed June, 08, 2020]. Available at: <https://www.analog.com/media/en/technical-documentation/application-notes/AN-940.pdf>.
- [69] Schweber B. *How to Choose and Use Precision Op Amps Effectively*. [Web article], 2019. [Online; accessed June, 08, 2020]. Available at: <https://www.digikey.com/en/articles/how-to-choose-and-use-precision-op-amps-effectively>.
- [70] Williams J. of Linear Technology Corp. *Application Note 21 – Composite Amplifiers*. [Application Note], 1986. [Online; accessed June, 08, 2020]. Available at: <https://www.analog.com/media/en/technical-documentation/application-notes/an21f.pdf>.
- [71] Teare S., editor. *Practical Electronics for Optical Design and Engineering*. The International Society for Optics and Photonics (SPIE), 1st edition, 2016.

- [72] Hamamatsu Photonics K.K. *Technical Information SD-12 – Characteristics and use of infrared detectors*. [Application Note], 2011. [Online; accessed May, 22, 2020]. Available at: https://www.hamamatsu.com/resources/pdf/ssd/infrared_kird9001e.pdf.
- [73] Maxim Integrated Products Inc. *AN6139 – Selecting the Right ADC for Your Application*. [Application Note], 2015. [Online; accessed June, 08, 2020]. Available at: <https://www.maximintegrated.com/en/design/technical-documents/tutorials/6/6139.html>.
- [74] Pelgrom M. *Analog-to-Digital Conversion*. Springer Science+Business Media LLC, 2nd edition, 2013.
- [75] Giovino B. *IoT Microcontrollers Have ADCs, but Know When to Choose and Apply an External ADC*. [Web article], 2018. [Online; accessed June, 09, 2020]. Available at: <https://www.digikey.com/en/articles/iot-microcontrollers-have-adcs-know-when-apply-an-external-adc>.
- [76] Maxim Integrated Products Inc. *AN748 – The ABCs of Analog to Digital Converters: How ADC Errors Affect System Performance*. [Application Note], 2002. [Online; accessed June, 09, 2020]. Available at: <https://www.maximintegrated.com/en/design/technical-documents/tutorials/7/748.html>.
- [77] Rohm Co. Ltd. *Electronics Basics – What is a DC/DC converter?* [Web tutorial]. [Online; accessed June, 09, 2020]. Available at: <https://www.rohm.com/electronics-basics/dc-dc-converters/linear-vs-switching-regulators>.
- [78] Ebermann M. et al. I3.1 - Design, Operation and Performance of a Fabry-Perot-Based MWIR Microspectrometer. In *Proceedings OPTO 2009 & IRS2 2009*, pages 233–238. AMA Association for Sensors and Measurement, 2009.
- [79] Drebuschak V. *The Peltier Effect*. *Journal of Thermal Analysis and Calorimetry*, 91(1):311–315, 2008.
- [80] Weremczuk J. et al. *Flexible coplanar line of low heat load to cooled infrared detector*. In *Procedia Engineering Vol. 120, EUROSENSORS 2015*, pages 1183–1186. Elsevier Ltd., 2015.
- [81] TEC Microsystems GmbH. *Thermoelectric Coolers Intro*. [Web tutorial]. [Online; accessed June, 09, 2020]. Available at: <https://www.tec-microsystems.com/faq/thermoelectric-coolers-intro.html>.

- [82] Vishay Dale Electronics Inc. *Document Number 33016 – NTC and PTC Thermistors*. [Application Note], 2002. [Online; accessed June, 09, 2020]. Available at: <https://www.vishay.com/docs/33016/engnote.pdf>.
- [83] Prodic A. & Maksimovic D. *Digital PWM controller and current estimator for a low-power switching converter*. In *COMPEL 2000. 7th Workshop on Computers in Power Electronics. Proceedings (Cat. No.00TH8535)*, pages 123–128, 2000.
- [84] Computer Language Company Inc. *Definition: control signal*. [Web article] published by Computer Language Company Inc. [Online; accessed June, 10, 2020]. Available at: <https://www.computerlanguage.com/results.php?definition=control+signal>.
- [85] Thakor M. et al. *Precise temperature control through Thermoelectric Cooler with PID controller*. In *2015 International Conference on Communications and Signal Processing (ICCSP)*, pages 1118–1122, 2015.
- [86] de Miguel S. et al. *Identification model and PI and PID controller design for a novel electric air heater*. *Automatika*, 58(1):55–68, 2017.
- [87] IEC 60115-8:2009. *Fixed resistors for use in electronic equipment. Part 8: Sectional specification - Fixed surface mount resistors*. Geneva: International Electrotechnical Commission, 2009. 84 p.
- [88] VIGO System S.A. *MCT Photovoltaic detectors – PVI-2TE*. [Datasheet], 2017. [Online; accessed June, 13, 2020]. Available at: <https://vigo.com.pl/produkty/pvi-2te/>.
- [89] Hamamatsu Photonics K.K. *InAsSb photovoltaic detectors – P13243 series*. [Datasheet], 2020. [Online; accessed June, 13, 2020]. Available at: https://www.hamamatsu.com/resources/pdf/ssd/p13243_series_kird1130e.pdf.
- [90] Analog Devices Inc. *LTC2057/LTC2057HV – High Voltage, Low Noise Zero-Drift Operational Amplifier*. [Datasheet], 2013. [Online; accessed June, 14, 2020]. Available at: <https://www.analog.com/media/en/technical-documentation/data-sheets/2057f.pdf>.
- [91] Texas Instruments Inc. *SLAA926A – Transimpedance amplifier circuit with MSP430TM smart analog combo*. [Application Note], 2020. [Online; accessed June, 14, 2020]. Available at: <https://www.ti.com/lit/an/slaa926a/slaa926a.pdf?ts=1592117224012>.

- [92] Analog Devices Inc. *ADN8833 – Ultracompact, 1 A Thermoelectric Cooler (TEC) Driver for Digital Control Systems, Rev. B*. [Datasheet], 2018. [Online; accessed Apr, 15, 2020]. Available at: <https://www.analog.com/en/products/adn8833.html>.
- [93] VIGO System S.A. *IR detectors user's guide*. [Application Note], 2018. [Online; accessed May, 22, 2020]. Available at: https://vigo.com.pl/wp-content/uploads/2018/07/IR_detectors_users_guide.pdf.
- [94] Texas Instruments Inc. *SNOAA12 – Methods to Reduce Thermistor Linearization Error, Memory, and Power Requirements Over Wide Operating Temperature Ranges*. [Application Note], 2018. [Online; accessed June, 14, 2020]. Available at: <https://www.ti.com/lit/an/snoaa12/snoaa12.pdf?ts=1592143688264>.
- [95] Texas Instruments Inc. *SLOA024B – Analysis of the Sallen–Key Architecture*. [Application Note], 2002. [Online; accessed June, 23, 2020]. Available at: <https://www.ti.com/lit/an/sloa024b/sloa024b.pdf>.
- [96] Sinha P., editor. *Speech Processing in Embedded Systems*. Springer US, 2009.
- [97] Texas Instruments Inc. *LP295x-N Series of Adjustable Micropower Voltage Regulators*. [Datasheet], 2017. [Online; accessed May, 22, 2020]. Available at: <https://www.ti.com/store/ti/en/p/product/?p=LP2951ACMM-3.3/NOPB>.
- [98] Carter B. & Mancini R. *Op Amps for Everyone, 5th Edition*. Newnes, an imprint of Elsevier Inc., 2017.

Appendix 1. MCU Pin Configuration

Pin #	Function	Schematic ID	Additional notes
1	VREF-	AGND	Analog ground reference point for the +2.5 V internal reference voltage OUTPUT
2	VREF+	VREF_2V5	Internal +2.5 V reference voltage OUTPUT from the MCU to the detector amplifier interface
3	A2	VREF_TEC_2V5	Measure the TEC driver's internal 2V5 reference, divided to 1.25 V by a resistor voltage divider
4	A12	DET_MEAS	Amplified measurement signal from the photodetector, DC offset +1.25 V
5	A13	I_TEC_MEAS	Voltage proportional to the current flowing through the thermoelectric cooler (from ADN8833)
6	A14	V_TEC_MEAS	Voltage over the thermoelectric cooler (from ADN8833)
7	A15	30V_MEAS	FPI driver circuit supply voltage
8	P4.7	TEC_ENABLE	ADN8833 TEC driver is enabled, when EN/SY input > 2.1 V and VLIM/SD input > 0.07 V
9	-	TP2	-
10	TB0.1	IR_PWM	Microglow IR source control voltage
11	TB0.2	FPI_PWM_1	FPI operating voltage 1
12	TDO	JTAG_TDO	-
13	TDI	JTAG_TDI	-
14	TMS	JTAG_TMS	-
15	TCK	JTAG_TCK	-
16	A8	NTC_MEAS	Voltage over the resistor linearizing the detector's NTC thermistor
17	A9	I_IR_MEAS	Voltage corresponding the current flowing through the microglow IR source
18	A10	V_IR_MEAS	Voltage over the microglow IR source
19	A11	12V_MEAS	-
20	-	TP6	-
21	-	TP7	-
22	TEST	TEST	-
23	RST	RST / 3.3V	-
24	UCA0TXD	TXD	-
25	UCA0RXD	RXD	-
26	-	TP5	-
27	-	TP15	-
28	-	TP26	-
29	-	TP3	-
30	-	TP4	-
31	TB0.3	FPI_PWM_2	FPI operating voltage 2
32	TB0.4	TEC_CTRL_PWM	Control signal for the ADN8833 TEC driver
33	P4.4	LED	Supply voltage for a red LED indicator
34	-	TP28	-
35	-	TP29	-
36	DVSS	AGND	-
37	DVCC	3.3V	-
38	P2.7	FPI_SW_CTRL	Control signal for the SPDT switch used to modulate between FPI_PWM_1 and FPI_PWM_2
39	UCA1STE	RE	-
40	UCA1CLK	DE	-
41	AVSS1	AGND	-
42	HFXIN	Z1	-
43	HFXOUT	Z1	-
44	AVSS2	AGND	-
45	-	TP9	-
46	-	TP14	-
47	AVSS3	AGND	-
48	AVCC	3.3V	-
49	THERM_PAD	AGND	Exposed / Thermal pad, connected to AGND